Determination of surface impurities by means of nuclear resonance interactions

W. Rudolph and C. Bauer

Central Institute of Physics Research, Rossendorf, Germany Democratic Republic
Fiz. Elem. Chastits At. Yadra **18**, 820–877 (July–August 1987)

The use of nuclear resonance reactions and resonance scattering processes for surface analysis of solids is demonstrated for many examples—from the technology of the production of electronic semiconductor devices to the investigation of geological and archeological samples. The modern tendencies in this field are associated with the use of various methods (analysis of prompt nuclear reactions, x-ray spectral analysis by ion excitation, nuclear spectrometry of Rutherford backward scattering, and more), which augment each other and simultaneously improve the analytic possibilities (sensitivity and lateral and depth resolution). The development of ion microbeams is of particular interest in this direction.

INTRODUCTION

Nuclear-physics methods of analysis are of undoubted importance for the determination of small numbers of atoms or nuclei. Activation analysis by means of neutrons, γ rays, or charged particles can be used particularly effectively to measure traces of impurities in the interior of a sample. On the other hand, prompt radiation analysis has specific advantages for the investigation of the surface regions of solids.

When a solid is bombarded with light ions with energies in the mega-electron-volt region, the target emits (during the irradiation process) x rays, nuclear radiation (charged particles, neutrons, and γ rays), and particles elastically or inelastically scattered by nuclei of the substrate.

These prompt radiations are characteristic of the atoms or nuclei emitting them and are the basis of analytic methods well known at the present time as PNRD (x ray analysis by ion excitation), NBS (nuclear spectrometry of Rutherford backward scattering), and PNRA (prompt nuclear-reaction analysis).[1] Using these methods, one can obtain information about the total concentration and depth distribution of a number of elements or isotopes in the surface region of solids. By using the channeling technique, one can also determine the localization of foreign atoms in the lattices of simple crystalline materials. These methods are therefore suitable when one is studying diffusion phenomena, the mechanisms of growth of thin films, and the contamination of the surface regions of solids as a function of the treatment of the substrate. Such investigations are of fundamental interest in solid-state physics, metallurgy, and electrochemistry, as well as in other disciplines in which there are surface reactions and atomic exchange processes.

Our interest is in prompt nuclear-reaction analysis. However, the scattered particles and ion-induced x rays also contribute to the spectra of charged particles and photons emitted by the target. The three methods, PNRA, PNRD, and NBS, can be used with almost exactly the same experimental equipment, it being merely necessary to change slightly the conditions of the measurements. These methods complement each other, and their common or even simultaneous use frequently leads to the acquisition of more comprehensive and detailed information about the surface region of the investigated substrate.

The emission of x rays can be induced by different ions. The characteristic x rays identify the atoms that emit them. For light incident ions, the x-ray intensities can be well described by the model of direct ionization with allowance for some corrections to the cross sections. When semiconductor detectors are used, it is possible to obtain good element resolution and simultaneously determine foreign atoms of a large number of elements.[2,3] Of course, x-ray emission following ion excitation is not a nuclear interaction process. In what follows, this method will not be considered.

Nuclear spectrometry of Rutherford backward scattering is used mainly to detect and determine the concentration profile of heavier atoms over the depth in a substrate consisting of lighter atoms and to analyze these distributions in simple crystals. For incident He ions with energies $E \lesssim 2$ MeV the interaction process is mainly purely Coulomb scattering, and the intensities of the scattered ions are well described by the Rutherford cross section.[4] Conversely, for low-energy protons, as well as for more energetic He ions, the nuclear potential makes an important contribution to the scattering process, and the cross section may have a resonance behavior.[4]

The analysis of prompt nuclear reactions is well suited to the determination of light elements in a matrix of heavier elements. However, in contrast to ion-induced x-ray emission and Rutherford scattering, a general theoretical description of the energies of the nuclear radiation and cross sections is impossible, and in analytic applications one must use experimental information about these quantities. In PNRA, protons and deuterons are mainly used as the incident ions. For these incident particles, the Coulomb barrier is relatively low. In this case, large cross sections for light nuclei are obtained already at low energies of the incident particles. For heavy target nuclei and low energies of the incident particles, the cross sections are very small, and, therefore, for heavy matrix elements one observes a low intensity of the background. The reactions induced by the ions of ^{3}He and ^{4}He or tritium (^{3}H) require a higher bombarding energy or specially equipped accelerators. In what follows, we shall restrict outselves primarily to incident protons and deuterons and detected charged final particles and γ rays. If the reaction is induced by incident particles with resonance energy, then one observes well-defined transitions of groups of particles and γ rays associated with the levels of the final nucleus. The behaviors of two isotopes of a given element are quite different. At low energies of the incident particles, as considered here, certain reactions are energetically possible in many cases only for one of the isotopes, and the other can be ignored, whatever its concentration. On this basis a spe-

 0090-4759/87/040350-26$04.40

cial technique has been developed in connection with prompt nuclear reactions to determine traces of elements using enriched stable isotopes.[5]

The intensities of the prompt-radiation components vary strongly with the energy of the incident ions. Moreover, the transitions of the different particles or γ rays exhibit different energy dependences. Particularly strong variations of the intensity and very narrow resonances are observed for many nuclear reactions induced by protons and for scattering processes. In these cases, reactions take place through the formation and decay of a highly excited nucleus. A much weaker energy dependence is observed in direct reactions. However, many experimental results can be excellently explained if one assumes that both of the considered cases contribute to the reaction mechanism. In nuclear processes induced by low-energy protons and deuterons the compound-nucleus mechanism is mainly dominant, and this leads to more or less narrow resonances. Sometimes they are superimposed on broader structures of the cross sections. Therefore, we also include in our treatment resonance reactions and processes that are characterized by these broader structures of the cross sections. Our approximation differs from that made by the authors of Ref. 6, who restrict this region to resonances with a width of a few kilo-electron-volts or less.

The nuclear physicists who used these energetic ions in the field of fundamental investigations had an excellent idea of the analytic power of these methods from the very beginning. They used the scattering of ions and nuclear reactions to determine the thicknesses of targets, contamination in thin films, and the formation of defects in a target during the time of irradiation, i.e., the parameters that influence the experimental results and their theoretical interpretation.[7] However, wide and effective use of these analytic methods began with the development of solid-state particle detectors and the possibility of photon detection.[8,9] These devices gave a good energy resolution, good linearity, rapid response, and the possibility of simultaneous detection of photons in a wide energy range. In the field of electronics, a different important improvement for the collection of data and their analysis appeared. In conjunction with solid-state detectors, multichannel analyzing devices, and microcomputers, accelerators were transformed into fast and effective analytic instruments.[1,2,5]

Today, ion scattering and prompt nuclear reactions are widely used to investigate surface regions and also sample depths above a few microns. Information obtained on the sample depth is based on the energy loss of charged particles [incident ions and (or) charged final particles] in the matter, and it is therefore no longer necessary to use the method of layer-by-layer removal. On the other hand, these methods are not absolutely nondestructive, since bombardment by ions produces defects and introduces new atoms; however, all these changes in the substrate are mainly concentrated at the end of the ion range.

Analysis of prompt nuclear reactions and nuclear spectrometry of Rutherford backward scattering are not such sensitive methods for analysis of surfaces as, for example, Auger electron spectroscopy and mass spectroscopy of secondary ions, but they can be used for depths up to several hundred nanometers or even to several microns in exceptional cases. Separation of the contributions of the surface and depth components to the measured signal (radiation yield of nuclei of a definite type) is possible only to within limits determined by the depth resolution. In favorable cases, values down to 10 nm or even less can be achieved for scattering and analysis by means of nuclear reactions. In addition, the experimental results do not depend on the chemical state, and they are not influenced by the binding effects that ensure the stability of the sample in vacuum and when bombarded by particles. Therefore, these methods make it possible to obtain the total concentration of the required atoms or nuclei in the surface region, whereas infrared spectroscopy gives information about the atoms in the bound states.

Nuclear resonance reactions and resonance scattering processes are analytic techniques that augment and extend the other analytic methods.

1. EXPERIMENTAL TECHNIQUE

1. Requirements on the ion beams and control of them

Figure 1 shows the general arrangement of an experiment. We shall consider only the main requirements on the ion beam and on the beam control elements, and we shall consider the chamber for the target, the detection, and the data-analysis system. We shall not dwell on the production and acceleration of the ions and on the energy stabilization arrangements. For all these questions, we refer to Refs. 5 and 10 and the bibliography given there.

Passing through the vacuum tube, the accelerated ions enter the magnetic analyzer, where the necessary ions are separated. The separated beam is then collimated and directed onto the target. By means of special detectors, the radiation emitted by the target is measured, an energy analysis is made, and the events are accumulated in a corresponding module. A microcomputer can be used to control the beam, vary the energy automatically, and analyze the measured spectra. The final stage includes separation of the background and determination of the energy and intensity of the radiation.

For the resonance-reaction method, one generally requires an ion beam of high stability with respect to the energy and the position of the beam spot on the target. For the determination of depth distributions by means of narrow resonances, the energy spread of the beam may make the main contribution to the total energy spread on the surface of the target and may, therefore, reduce the energy resolution. In addition, the ion energy must vary within a given range to enable one to exploit the resonance energies. In the majority of cases, one can use different gases in the ion source and, thus, obtain and accelerate different ions.

Usually, variation of the energy is achieved by varying the magnetic field of the analyzing magnet and using automatic adjustment of the energy to enable selective incident particles to pass through the magnetic analyzer. In Ref. 5 there is a description of an automatic energy-scanning system based on the use of special deflecting plates before and after the analyzing magnet. The system makes possible energy scanning for fixed intensities of the analyzer magnetic field, and an influence of the hysteresis effect can be eliminated.

For prompt radiation analysis, the beam currents usually vary from a few nanoamperes to microamperes,

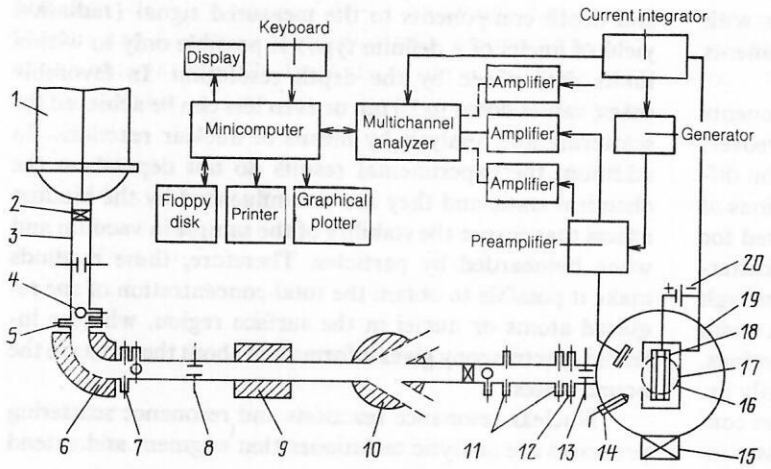

FIG. 1. Scheme of a typical experimental facility, including beam control system, chamber for target, and electronic devices: 1) ion accelerator; 2) valve; 3) vacuum tube; 4) quartz screen; 5) entrance collimator; 6) analyzing magnet; 7) collimator; 8) control plates; 9) magnetic quadrupole lenses; 10) deflecting distributing magnet; 11) collimators, diaphragms; 12) antiscattering diaphragm; 13) electron delay; 14) sputtering source; 15) vacuum lock for target; 16) γ-ray detector; 17) secondary-electron delay screen; 18) multiposition target support; 19) target chamber; 20) electron delay voltage.

these being determined primarily by the yield of the reactions and the stability of the target. The area of the beam spot on the target is 1 mm^2. Using special collimators and a precision system for forming the beams for measurement of distributions on the surface,[11,12] microbeams with a beam spot on the target with diameter down to 1 μm were obtained. Besides the analyzing magnet, quadrupole lenses, and collimating devices, the control system includes deflecting plates for centering the beam and special antiscattering diaphragms to suppress the beam halo. If the measurement is completed, the beam is interrupted, and it does not reach the target. It should be noted that the collimators in the immediate vicinity of the target may themselves be a source of the background, particularly in the case of γ spectroscopy.

2. Target chamber

The radiation intensities are determined relative to the number of particles incident on the target during the time of measurement. If the target chamber is well insulated, it can be used as a Faraday cylinder, and the exposure on the sample will be determined by integrating the beam current. In the case of unavoidable electrical contact of the chamber with other parts of the equipment, such as pumps and other peripheral devices, the ion charge accumulated in the process of the measurements is determined by integrating the current on the insulated target support, which is surrounded by matter that effectively suppresses secondary electrons. Valuable comments on exact measurements of the exposure are given in Ref. 10.

The target chamber contains a multiposition support for the targets, a trap with cooling liquid nitrogen, and charged-particle detectors. The target can be placed relative to the beam spot from outside. To avoid penetration of air, the completely prepared support of the samples is rapidly changed through a vacuum lock. The analysis is usually made at beam angles of incidence $\theta_1 = 45$ or 0° relative to the normal to the target. Reduction to grazing collisions ($\theta_1 \approx 70$–80°) leads to an improvement of the depth resolution and analysis sensitivity for a thin surface layer. In this connection, problems can arise through roughness of the sample surface.

Contaminations that accumulate on the surface of the target during the process of irradiation can have a strong influence on the analytic results, especially on the sensitivity limits for a number of elements. Therefore, the construction of the chamber must include measures to exclude sources of contamination. In addition, cooling by liquid nitrogen must be used to reduce the hydrocarbon vapor pressure in the vicinity of the target. In practice, the most acceptable chambers for the target are based on superhigh vacuum technology with propellerless pumps. Measurements are made at a pressure of order 10^{-4}–10^{-6} Pa. In exceptional cases, these chambers can be heated to 400 °C. Important improvements are cooling and heating of the target for special investigations and a purifying device.

3. Detection system

Particle spectra are usually obtained by means of surface-barrier silicon detectors placed at large angles. The detectors are chosen in accordance with the aims of the analysis.[5,10] In the best case, several detectors are placed simultaneously around the sample. When nuclear reactions are used, additional absorbers in front of the detectors are often not capable of suppressing the elastically scattered incident ions. It must be possible to change the different absorbers from outside.

For measurements of γ rays, the detectors can be placed outside the chamber. Gamma rays can pass through relatively thick aluminum windows. Of course, for low-energy γ rays it is necessary to take into account the effects of absorption. In the majority of cases, Ge(Li) detectors with high resolution are used at short distances from the target to ensure a high yield of γ rays and good detection sensitivities. If a good energy resolution is not required, it is preferable to use high-efficiency large-volume detectors based on NaI. To analyze γ rays of very low energies, it is necessary to use detectors based on superpure germanium with high energy resolution ($\Delta E \lesssim 500$ eV for 100 keV). To avoid the effects of strong absorption, these detectors are joined directly to the chamber for the target, or one uses a chamber with very thin windows. The efficiency of the high-resolution germanium detectors depends strongly on the energy of the γ rays and must be determined experimentally if it is necessary to make absolute measurements. In the majority of cases, measurements with high accuracy can be made by using reference targets whose thickness is well known.

In accordance with the adopted scheme for transmitting the signal (see Fig. 1), the amplified voltage pulses are

analyzed by analog-to-digital converters and then are sent to a multichannel memory. Both quantities are integrated in the multichannel analyzer. The spectra can be recorded on magnetic tape or floppy disks. To analyze the spectra, control the beam, and change the energy automatically, and also to adjust the target, a microcomputer is used, this being part of an industrial analyzing facility. To obtain reliable spectra, superposition effects are eliminated by restricting the counting rate or by using rejection of superpositions. A correction for the detection dead time must also be introduced. Usually, this is done automatically, a test pulse, which is detected by the current integrator, being sent to the amplifier.

4. Stability of the targets

During bombardment by the ions, the sample receives a fairly high energy, and this leads to heating of the target. Then the breaking of the chemical bonds by the cascade of collisions induced by the incident ions can lead to the formation of volatile components. Both effects can influence the composition of the target, particularly in the surface region. Therefore, the beam current and beam current density must be varied in a way that guarantees stability of the target.

Effects of the formation of charges on the surface of the insulator can be avoided by means of thin conducting films deposited on the substrate. Another method is to use an external ion beam to investigate biological samples containing a large number of volatile components.[13] In this case, the beam is admitted through a thin foil depending on the analytic task. Because of the effects of the energy spread in this foil, this procedure cannot be used to determine depth profiles by means of resonance reactions.

2. BASIC CONCEPTS OF SURFACE ANALYSIS

1. Spectra and yield functions

The radiation spectra measured at fixed energies of the incident particles, together with the yield functions, are used to analyze the surface regions of solids. The yield curve is the intensity of a definite radiation component as a function of the energy of the incident particles. We shall consider some experimental spectra and yield functions obtained in reactions induced by protons and deuterons.

Figure 2 shows the γ-ray spectrum from a thick silicon target irradiated with 0.93-MeV deuterons. The target was covered by an oxide film with added carbon. A complicated γ-ray spectrum is observed. Most of the γ rays are due to decay of the excited ^{29}Si nucleus produced in the $^{28}\mathrm{Si}(d, p)^{29}\mathrm{Si}$ reaction. Thus, the transition energy $E_\gamma = 4.934$ MeV noted in Fig. 2 corresponds to decay of the level with energy $E_x = 4.934$ MeV of the ^{29}Si nucleus. The presence of oxygen and carbon impurities leads to γ transitions with energies E_γ equal to 0.871 and 3.086 MeV, which arise in the $^{16}\mathrm{O}(d, p\gamma)^{17}\mathrm{O}$ and $^{12}\mathrm{C}(d, p\gamma)^{13}\mathrm{C}$ reactions, respectively; this is also noted in Fig. 2.

For comparison, Fig. 3 gives the spectra from a silicon target bombarded by deuterons with energies 0.93 and 0.75 MeV, respectively. To suppress the elastically scattered incident particles, an additional absorber made of mylar of 11-μm thickness was used. Figure 3 shows several proton groups formed in the $^{28}\mathrm{Si}(d, p)^{29}\mathrm{Si}$ reaction. Here, the group p_{10} corresponds to the ^{29}Si state with energy 4.934 MeV which leads to the strong γ transition shown in Fig. 2. The carbon and oxygen impurities on the surface are manifested in relatively narrow groups of particles induced by the $^{12}(d, p)^{13}\mathrm{C}$ and $^{16}\mathrm{O}(d, p)^{17}\mathrm{O}$ reactions, respectively. In contrast, the thick silicon substrate gives broad groups of particles that can be observed especially in the case of the group p_{10}. This broadening is due to the deceleration of the incident and final particles through the energy dependence of the cross sections for the different final states of ^{29}Si. Comparison of the spectra measured at energy E_d equal to 0.93 and 0.75 MeV shows that the radiation intensities depend strongly on the energy of the incident particles. At lower energies of the incident particles, the background is reduced in the region of the oxygen and carbon peaks, and better detection limits can be obtained. The same is true for the detection of the γ rays. Figure 4 shows parts of the γ-ray spectrum measured for a thick silicon target at energy E_d equal to 1.475 and 1.017 MeV, respectively. Only the energy region near the γ-ray peak with energy 871 keV from the $^{16}\mathrm{O}(d, p\gamma)^{17}\mathrm{O}$ reaction is shown. At a lower energy of the incident particles, the background is strongly reduced, while the intensity of the oxygen peak is not reduced so much.

The background depends strongly on the material of the substrate. For heavy target nuclei and at low energies of the incident particles the nuclear reactions have a very low

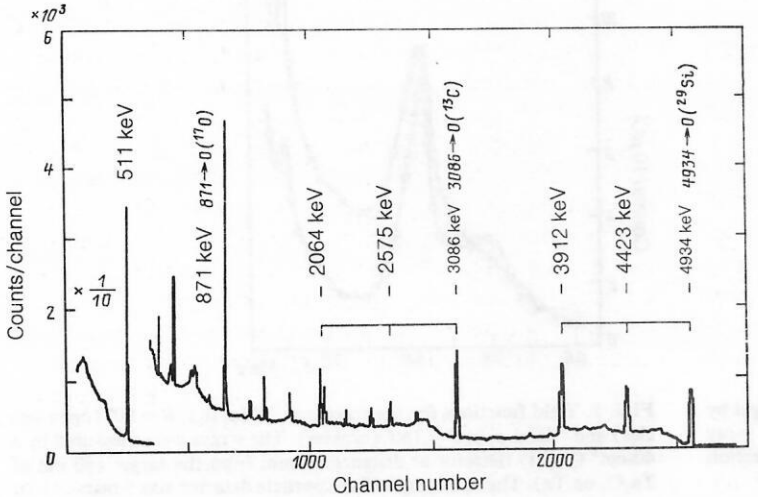

FIG. 2. Spectrum of γ rays obtained by means of a thick silicon target irradiated with 0.93-MeV deuterons.[72]

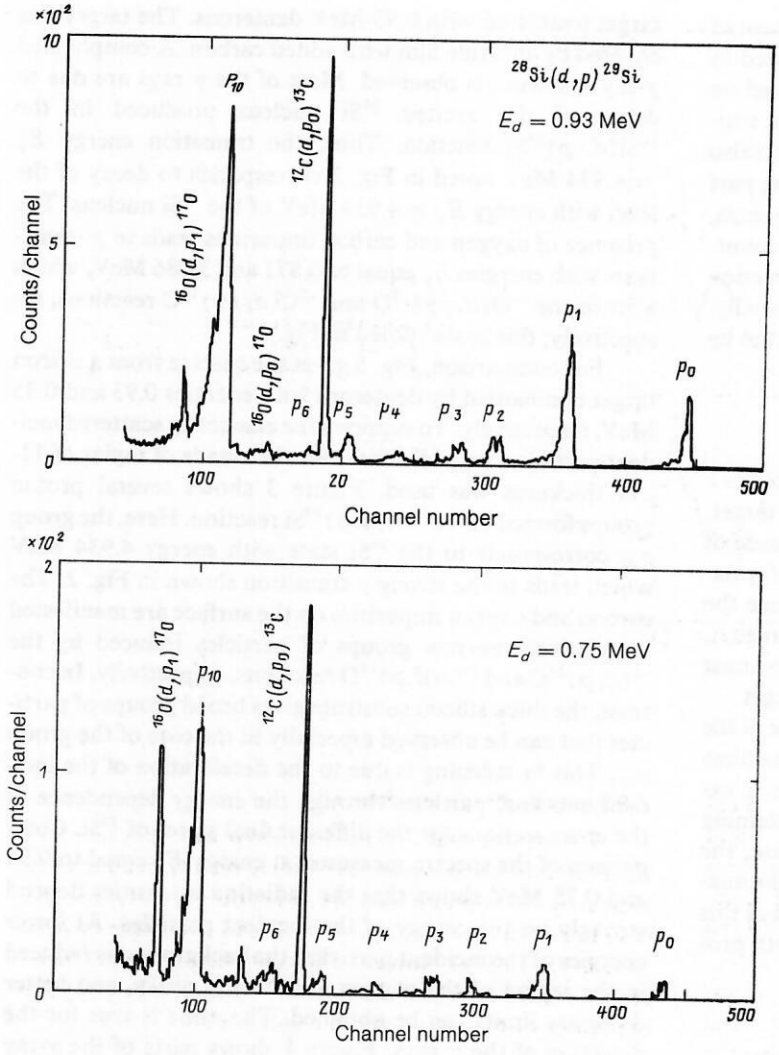

FIG. 3. Spectrum of protons emitted by a thick silicon target bombarded with deuterons with energies 0.93 and 0.75 MeV [$^{28}Si(d,p)^{29}Si$ reaction].

yield because of the high Coulomb barrier. Therefore, nuclear reactions are well suited for the determination of light atoms in a heavy matrix.

As already noted the reaction yield for the determined nucleus also depends on the energy of the incident particles. As an example, Fig. 5 gives the yield curves of the $^{16}O(d, p_1)^{17}O$ and $^{16}O(d, p\gamma)^{17}O$ reactions, respectively, for the range of deuteron energies $E_d = 0.6$–1.35 MeV. The two curves were measured simultaneously using a silicon sur-

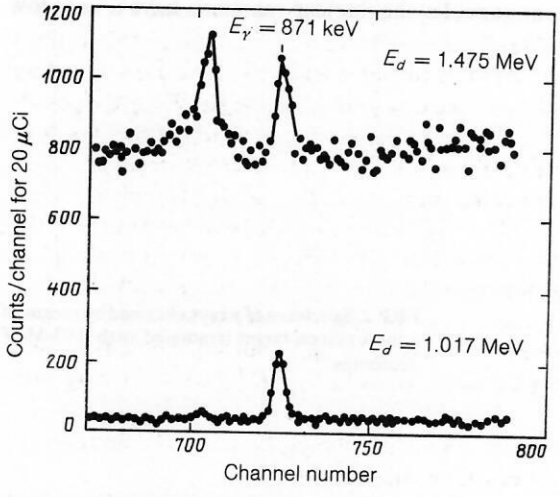

FIG. 4. Spectrum of γ rays due to irradiation of a thick silicon target by deuterons with energies 1.475 and 1.017 MeV, respectively. The γ-ray peak with energy 871 keV arises by virtue of the $^{16}O(d, p\gamma)^{17}O$ reaction from the surface film of natural oxide.[72]

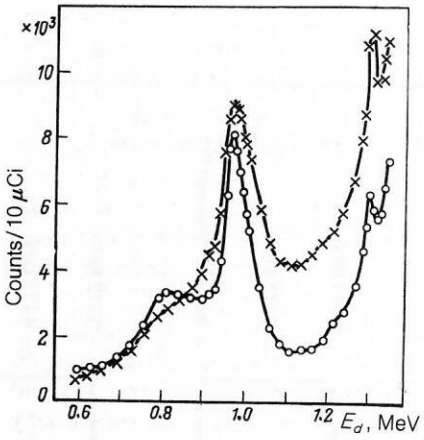

FIG. 5. Yield functions for the reactions $^{16}O(d, p_1)$, $\theta = 90°$ (open circles) and $^{16}O(d, p\gamma)$, $\theta = 150°$ (crosses). The γ rays were measured by a 40-cm³ Ge(Li) detector at distance 40 mm from the target (80 nm of Ta_2O_5 on Ta). The solid angle of the particle detector was 9 msr.

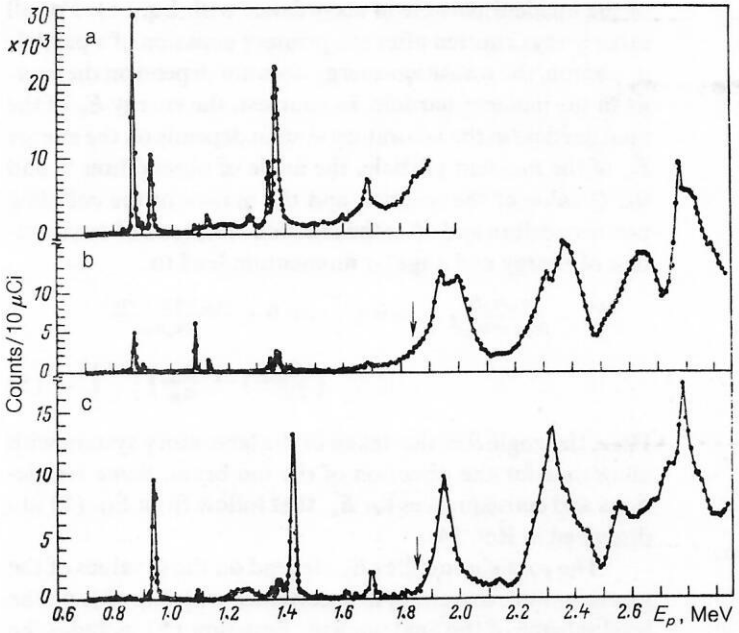

FIG. 6. Yield functions of the $^{19}F(p, \alpha\gamma)^{16}O$ and $^{19}F(p, p'\gamma)^{19}F$ reactions for different γ transitions measured using a 20-nm CaF_2 target and a Ge(Li) detector[36]: a) $^{19}F(p, \alpha\gamma)$, $E_\gamma = 3$–7.2 MeV; b) $^{19}F(p, p'_1\gamma)$, $E_\gamma = 197$ keV; c) $E = 110$ keV.

face-barrier detector and a Ge(Li) detector, and the measurements were made at detection angles θ equal to 150 and 90°. It is obvious from the comparison of the yield functions and the particle spectra in Fig. 3 that the conditions of detection for oxygen on silicon are better at $E_d = 0.75$ MeV than at the higher deuteron energy $E_d = 0.93$ MeV, despite the much higher radiation yield. In choosing the optimal conditions, one must take into account not only the background produced by reactions on the substrate nuclei but also the reaction yield for the investigated nucleus, which depends on the energy.

In the deuteron-induced reactions considered here, relatively broad structures of the cross sections are observed. In contrast, the proton-induced reactions are often characterized by a much stronger energy dependence of the radiation yields. As an example, Fig. 6 gives the yield functions obtained by proton bombardment of a thin CaF_2 target. The $^{19}F(p, p')^{19}F$ and $^{19}F(p, \alpha\gamma)^{16}O$ reactions lead to the appearance of low-energy ($E_\gamma = 110$, 197 keV) and high-energy ($E_\gamma = 6.13$–7.15 MeV) γ rays. Their intensities were measured at 90° to the direction of the beam using a large (80 cm^3) Ge(Li) detector. For E_γ equal to 110 and 197 keV the resultant intensities are shown, whereas for the $(p, \alpha\gamma)$ reaction the integrated yield in the wide energy window $E_\gamma = 3$–7.5 MeV is shown. For $E_p \lesssim 1.5$ MeV more or less narrow isolated resonances are observed. At higher energies of the incident particles, the resonances are broadened and overlap. The same resonance gives very different yields for several γ transitions.

As has been shown, the radiation yields depend strongly on the energy of the incident ions and on the chosen radiation component corresponding to a definite reaction and (or) state of the final nucleus. We shall now consider briefly some of the main aspects of the radiation energy and the radiation intensities as functions of the energy of the incident particle and the individuality of the target. For more details, we refer to the textbook of Ref. 14.

2. Radiation energy and intensity

We assume that the incident ion a with kinetic energy E_a in the laboratory system is incident on a target nucleus A, which, by assumption, is at rest and in the ground state. If E_a is so large that the incident particle can overcome or penetrate both the Coulomb and the centrifugal barrier, then a highly excited compound nucleus C^* with total energy E in the center-of-mass system can be formed:

$$E = E(C^*) = (m_A + m_a)c^2 + E'_a, \quad (1)$$

$$E'_a = \frac{m_A}{m_A + m_a} E_a.$$

Here, c is the speed of light and m_i are the nuclear masses of the colliding partners. This compound state can decay with the emission of γ rays to lower states of the same nucleus C or with the emission of a particle, this leading to the formation of various neighboring nuclei. The γ-ray emission scheme is shown in Fig. 7, in which the possible final configurations are characterized by the level schemes of the corresponding heavy nuclei and the c.m.s. kinetic energies E' of the colliding partners. The absolute energies of the ground states of the different configurations are given as rest-mass energies; they are indicated on the energy axis. In the nuclear reactions, the total energy is conserved, and all transitions of the particles and γ rays from the compound state to levels below the broken horizontal line in Fig. 7 are energetically allowed. Therefore, the compound state can decay by:

i) secondary emission of the incident particle as a result of elastic ($E^A_x = 0$) or inelastic ($E^A_x > 0$) scattering processes;

ii) primary emission of γ rays, leading to a capture reaction characterized by final nucleus C;

iii) emission of some final particle $b \neq a$ forming a final nucleus $B \neq A$. These processes are usually called mutually interchangeable collisions.[14] As is shown in Fig. 7, in the majority of cases several transitions to different levels of the

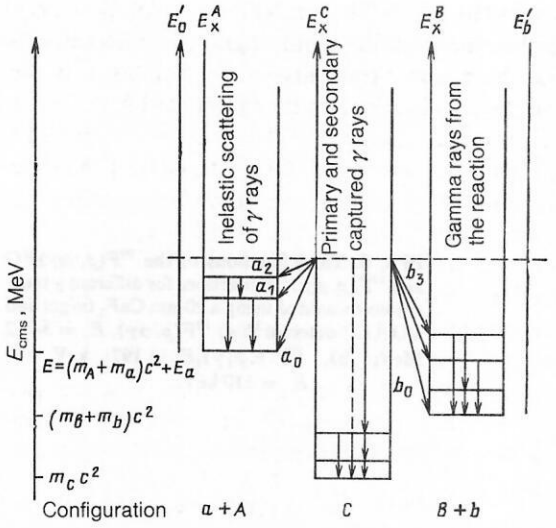

FIG. 7. Particle and γ-ray emission schemes in decay of a compound state.

same final nucleus are possible. The excited states give up their energy through the emission of the γ rays until the ground state is reached. In accordance with reactions of singular type, these forms of radiation are called inelastic scattering, capture, and γ-ray reactions. It should be noted that a level of the final nucleus can be populated by direct transitions from the compound state and (or) by additional γ transitions from highly excited states of the final nucleus.

Bearing in mind the reaction mechanism, the nuclear reaction for the two bodies can be written in the form

$$a + A \rightarrow C^* \rightarrow B + b + Q. \tag{2}$$

Here, the energy released or absorbed in the reaction is characterized by the value Q, which is defined as

$$Q = (m_A + m_a - m_B - m_b)\,c^2 - E_x^B = Q - E_x^B, \tag{3}$$

if the residual nucleus is formed in state a with excitation energy E_x^B. The nuclear reactions may be exothermic ($Q>0$) or endothermic ($Q<0$). For an endothermic reaction there exists a threshold energy, below which the reaction cannot take place.[14]

The measurements of the radiation are made in the laboratory system, and therefore the energy of the radiation and the intensity must be described in the same system. The energies of the γ rays correspond to the transition energies or the energy spacings $\Delta E = E_i - E_f$ of the initial and final states between which the γ transitions take place. However, the recoil effect and the Doppler effect lead to a small splitting of the energies, and the measured γ-ray energy is given by the expression[14]

$$E_\gamma = \left(\Delta E - \frac{\Delta E}{2mc^2}\right)\left(1 + \frac{v}{c}\cos\psi\right) \tag{4}$$

Here, m and v are the mass and velocity of the emitting nucleus, and the detection angle ψ is measured relative to the direction of motion of this nucleus. For fixed geometry of the experiment, one determines the photons from the final nuclei with very varied recoil directions. This can be manifested in an additional Doppler broadening of the γ peaks.

For the primary γ rays emitted when the compound state decays, the transition energy ΔE depends on the energy of the incident particle in accordance with Eq. (1). For all other γ rays emitted after the primary emission of a particle or photon, the transition energy does not depend on the energy of the incident particle. In contrast, the energy E_b of the final particle in the laboratory system depends on the energy E_a of the incident particle, the angle of observation θ, and the Q value of the reaction and the masses of the colliding partners before and after the reaction. The laws of conservation of energy and angular momentum lead to

$$E_b = \frac{m_a m_b E_a}{(m_B+m_b)^2}\left\{\cos\theta \pm \left[\cos^2\theta + \frac{m_B(m_B+m_b)}{m_a m_b}\left(\frac{Q}{E_a}+1-\frac{m_A}{m_B}\right)\right]^{1/2}\right\}^2. \tag{5}$$

Here, the angle θ is also taken in the laboratory system with allowance for the direction of the ion beam. Some restrictions and consequences for E_b that follow from Eq. (5) are discussed in Ref. 14.

The particle energies E_b depend on the Q values of the reactions and, therefore, in accordance with Eq. (3), on the level scheme of the final nucleus. Equation (5) includes the cases of elastic and inelastic scattering ($m_B = m_A$, $m_b = m_a, Q_0 = 0$) and capture ($m_b = 0$, $m_B = m_A + m_a$, $E_b = E_\gamma$).

For the regions of low energies of the incident particles and a number of final states, Eq. (5) can be replaced by the linear approximation

$$E_b = K_{ab}E_a + k \tag{6}$$

in order to describe E_b as a function of E_a. This approximation leads to a simple representation of the ratio of the energy to the depth for the final charged particles in thicker targets.

For well-defined energy E_a of the incident particles and detection angle θ, Eq. (5) leads to narrow intervals of the particle energies E_b. However, the assumption of good knowledge of the energy of the incident particles may be valid only for the surface of the sample and not within it. Because of the energy-loss processes, the energies of ions that have penetrated into the target and of the final particles emitted from the surface depend on the depth (Fig. 8). The incident particles collide with the surface of the target with energy E_0. At depth x, the final particles with energy $E_b(x)$ are generated by ions with energy $E_a(x)$. Along $l_2 = x/\cos\theta_2$, the final charged particles again lose energy and emerge from the surface with energy $E(x)$.

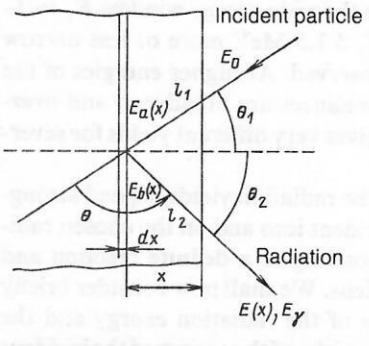

FIG. 8. Geometry of particle trajectories in the target. The nuclear reaction takes place at depth x, resulting in an energy loss of the incident particles and the charged reaction products.

For thin layers, the energy loss ΔE along the path Δx can be approximated as follows[14]:

$$\Delta E = NS(E)\,\Delta x, \tag{7}$$

where the energy-dependent cross section $S(E)$ is usually expressed in units of eV/(10^{15} atom/cm^2). The atomic density N of the atoms must then be expressed in units of 10^{15} atom/cm^3. The stopping power and the corresponding conversion of $S(E)$ for individual elements are given in Ref. 15. In complicated materials, the individual components i contribute to the energy loss in accordance with their stopping cross sections $S_i(E)$ and atomic densities N_i (Bragg rule):

$$\Delta E = \Delta x \sum_i N_i S_i(E) \equiv \Delta x\, N_M S_M(E). \tag{8}$$

Here, N_M is the total atomic density of the material of the substrate and $S_M(E)$ is the total stopping cross section.[15]

Taking into account the geometrical conditions (see Fig. 8) and expressing the energy loss in terms of the stopping cross sections [see Eq. (7)], we can represent the energy-to-depth ratio for the final charged particles in the form

$$E(x=0) - E(x) = N(x)\left\{\frac{K_a S_a(\bar{E}_a)}{\cos\theta_1} + \frac{S_b(\bar{E}_b)}{\cos\theta_2}\right\}. \tag{9}$$

Here, the stopping cross sections S_a and S_b correspond to the initial and final particles, respectively. In the range of depths in which we are interested, the mean energies $\bar{E}_a$ and $\bar{E}_b$ can be used to calculate these stopping cross sections. Strictly speaking Eq. (9) describes the mean difference between the energies of final charged particles formed on the surface $x = 0$ and at depth x, respectively. For the primary γ rays, the condition $S_b = 0$ is satisfied, and therefore only the retardation of the incident particles affects the radiation energy.

At excitation energies of mega-electron-volt order, ionization of the electron shells determines the contribution to the energy loss of the charged particles. These interactions give rise to only small-angle deflections of heavy incident particles. However, with increasing depth the statistical nature of the energy exchange is manifested both in an increase in the energy and in the energy straggling, and as a result the energy distribution of the ions is broadened. The energy spread (energy straggling) has a strong influence on the energy resolution and the depth resolution and it must be taken into account in a calculation of the depth profiles on the basis of measured spectra or yield functions. We refer to the textbook of Ref. 14 and to Ref. 4.

As can be seen from Fig. 8 and Eq. (9), the energies $E_a(x)$ and $E(x)$ depend on the ranges l_1 and l_2 in the target. Taking into account the geometrical conditions illustrated in Fig. 8, the intensity or differential yield $dY(\theta, E_a, E)$ of the radiation component (of a group of particles or γ transitions selected for determination of nuclei of type A) formed in a thin layer dx at depth x and emitted from the surface with energy $E(x)$ is described by the expression

$$dY(\theta,\ E_a(x),\ E(x)) = \varepsilon n N_A(l_1)\,\sigma(\theta_1,\ E_a(l_1)) \times \exp\left(-\mu l_1 \frac{\cos\theta_1}{\cos\theta_2}\right) dl_1 = y(\theta,\ E_0,\ x)\,dx. \tag{10}$$

The depth coordinate $l_1 = x/\cos\theta_1$ is chosen in the direction of incidence of the ion beam. The exponential function describes the absorption of the γ rays. Emission of particles is characterized by $\mu = 0$. The total efficiency ε of the experimental facility includes the solid angle, the detector efficiency, and the window transmission coefficients; n is the exposure to the ions incident on the target, and $N_A(x)dx$ is the number of nuclei of type A in the target per 1 cm^2. The differential cross section $\sigma(\theta, E_a)$ is averaged over the solid angle, and is measured in barns per steradian. In what follows, we shall ignore the absorption of the γ rays.

Taking into account the depth distribution $N_A(x)$ and the connection between the incident energy E_0 and the depth-dependent incident and produced particles, the differential yield is a function of E_0 and x, as noted in Eq. (10). Particles from dx at depth x leave the surface with energies in the interval $E(x)\ldots E(x) + dE$, and the ideal energy spectrum is described by the formula

$$y(\theta,\ E_0,\ E)\,dE = y(\theta,\ E_0,\ x)\left|\frac{dx}{dE}\right| dE. \tag{11}$$

Here, the geometrical factors are contained in the coefficient dx/dE. These quantities are considered in Sec. 3 for the final charged particles and primary γ rays.

The real spectra are obtained from Eq. (11) by taking into account the effects of the energy spread and the finite resolution of the detector. The particle spectra obtained in the case of bombardment of a thick silicon target by deuterons with $E_d = 0.93$ and 0.75 MeV (see Fig. 3) illustrate the influence of the energy of the incident particles on the measured energy distribution. One can see particularly clearly the shift of the sharp part of the peak to higher energies in the case of the p_{10} group. Because of the constant atomic density of the silicon, the decreasing yield at lower final energy reflects the energy dependence of the cross section.

Equation (11) describes the ideal energy distribution of the radiation component, whose energy depends on the depth. However, for the secondary γ rays the transition energies are constant and depend on the depth at which they occur. Therefore, for these γ rays only the integrated yield can be measured:

$$V(\theta,\ E_0) = \int_0^{x_{\max}} y(\theta,\ E_0,\ x)\,dx, \tag{12}$$

and it is equal to the area of the γ peak. Here, the energy width of the peak depends on the detector resolution and on the recoil and Doppler effects. The quantity $x_{\max}$ can be bounded by a finite depth distribution, $N_A(x) = 0$ for $x > x_{\max}$, or by the range of the incident ions in the given material of the substrate. For the radiations whose energies depend on the depth, the total yield is obtained by an analogous integration of Eq. (11) between the limits $E_{\max}$, equal to $E(x=0)$, and $E_{\min}$, these depending on the depth profile or the energy interval of the incident particles. For a number of reactions, $E_{\min}$ can also be bounded by the range of the final particle.

As is shown in Eq. (12), the total yield depends on the energy of the incident ion. This yield function can also be used for surface analysis. For thin targets, the yield curve reflects the energy dependence of the partial cross section $\sigma(\theta, E_0)$. This is shown in Figs. 5 and 6 for reactions induced by protons on the target nuclei ^{16}O and ^{19}F, respectively. Knowledge of the behavior of the cross section is needed to choose the optimum of the incident-particle energies, but

TABLE I. Values of Q_0 for proton-induced nuclear reactions and the excitation energies E_x for the lowest states of the corresponding final nuclei.[18–23]

Target nucleus	(p, p') reactions		(p, γ) reactions			(p, α) reactions			(p, n) reactions		
	E_1, MeV	E_2, MeV	Q_0, MeV	E_1, MeV	E_2, MeV	Q_0, MeV	E_1, MeV	E_2, MeV	Q_0, MeV	E_1, MeV	E_2, MeV
^{6}Li	2.185 *	3.563 *	5.606	0.429	4.57	4.020	—	—	−5.070	—	—
^{7}Li	0.478	4.630	17.255	2.90 *	—	17.347	—	—	−1.644	0.429	4.57
^{9}Be	1.680 *	—	6.585	0.718	1.740	2.125	2.185 *	3.563 *	−1.850	1.6	2.361
^{10}B	0.718	1.740	8.691	2.000	4.319	1.146	0.429	—	−4.434	3.351	5.22
^{11}B	2.125	4.445	15.957	4.439	7.654	8.590	2.90 *	—	−2.764	2.000	4.319
^{12}C	4.439	7.654	1.943	2.365 *	—	−7.552	1.6	2.361	−18.120	0.960	1.189
^{13}C	3.089	3.685	7.551	2.313	3.948	−4.063	0.718	1.740	−3.003	2.365 *	—
^{14}C	6.094	6.590	10.207	5.270	5.299	−0.784	2.125	4.445	−0.626	2.313	3.948
^{14}N	2.313	3.948	7.297	5.183	5.241	−2.922	2.000	4.319	−5.927	5.17	5.92
^{15}N	5.270	5.299	12.128	6.049	6.130	4.966	4.439	7.654	−3.536	5.183	5.241
^{16}O	6.049	6.130	0.600	0.495	3.104	−5.219	2.365 *	—	−16.211	0.194	0.424
^{17}O	0.871	3.055	5.607	0.937	1.042	1.191	2.313	3.948	−3.544	0.495	3.104
^{18}O	1.982	3.555	7.933	0.110	0.197	3.980	5.270	5.299	−2.438	0.937	1.042
^{19}F	0.110	0.197	12.845	1.634	4.248	8.114	6.049	6.130	−4.021	0.238	0.275
^{23}Na	0.440	2.076	11.690	1.369	4.123	2.378	1.634	4.248	−4.841	0.451	2.051
^{24}Mg	1.369	4.123	2.271	0.452	0.945	−6.881	0.332	1.716	−14.661	0.439	0.514
^{25}Mg	0.585	0.975	6.306	0.228	0.417	−3.143	0.583	0.657	−5.060	0.452	0.945
^{26}Mg	1.809	2.938	8.271	0.844	1.014	−1.819	0.440	2.076	−4.787	0.228	0.417
^{27}Al	0.844	1.014	11.586	1.779	4.617	1.600	1.369	4.123	−5.591	0.781	0.957
^{28}Si	1.779	4.617	2.747	1.384	1.954	−7.714	0.452	0.945	−15.114	0.106	0.878
^{29}Si	1.273	2.028	5.600	0.677	0.709	−4.822	0.228	0.417	−5.727	1.384	1.954
^{30}Si	2.235	3.499	7.297	1.266	2.234	−2.373	0.844	1.014	−5.010	0.677	0.709
^{31}P	1.266	2.234	8.865	2.230	3.778	1.916	1.779	4.617	−6.178	1.249	2.236
^{32}S	2.230	3.778	2.277	0.811	1.987	−4.202	1.384	1.954	−13.470	1.0	1.4
^{33}S	0.841	1.966	5.141	0.146	0.461	−1.517	0.677	0.709	−6.365	0.811	1.987
^{34}S	2.127	3.303	6.372	1.219	1.763	−0.628	1.266	2.234	−6.275	0.146	0.461
^{36}S	3.291	3.346	8.385	1.727	3.087	0.535	1.432	1.848	−1.927	3.291	3.346
^{35}Cl	1.219	1.763	8.507	1.970	4.178	1.866	2.230	3.778	−6.747	1.184	1.750
^{37}Cl	1.727	3.087	10.242	2.168	3.377	3.034	2.127	3.303	−1.596	1.410	1.611

*These states of the final nucleus are unbound and can decay with emission of particles.

TABLE II. Value of Q_0 for deuteron-induced reactions and excitation energies E_x for the lowest states of the corresponding final nuclei.[18–23]

Target nucleus	(p, p') reactions			(p, α) reactions			(p, n) reactions		
	Q_0, MeV	E_1, MeV	E_2, MeV	Q_0, MeV	E_1, MeV	E_2, MeV	Q_0, MeV	E_1, MeV	E_2, MeV
^{2}H	4.033	—	—	—	—	—	3.269	—	—
^{3}He	18.354	—	—	—	—	—	—	—	—
^{6}Li	5.026	0.478	4.630 *	22.373	—	—	3.382	0.429	4.57 *
^{7}Li	—0.192	0.981	2.255 *	14.23	—	—	15.031	2.90 *	—
^{9}Be	4.587	3.368	3.958	7.151	0.478	4.630 *	4.361	0.718	1.740
^{10}B	9.231	2.125	4.445	17.821	2.90 *	—	6.466	2.000	4.319
^{11}B	1.145	0.953	1.674	8.031	1.680 *	2.429 *	13.732	4.439	7.654
^{12}C	2.722	3.089	3.685	—1.341	0.718	1.740	—0.281	2.365 *	—
^{13}C	5.952	6.094	6.590	5.168	2.125	4.445	5.326	2.313	3.948
^{14}C	—1.007	0.740	3.105	0.361	0.953	1.674	7.983	5.270	5.299
^{14}N	8.609	5.270	5.299	13.574	4.439	7.654	5.073	5.183	5.241
^{15}N	0.267	0.120	0.297	7.687	3.089	3.685	9.903	6.049	6.130
^{16}O	1.920	0.871	3.055	3.110	2.313	3.948	—1.624	0.495	3.104
^{17}O	5.820	1.982	3.555	9.799	5.270	5.299	3.382	0.937	1.042
^{18}O	1.732	0.096	1.472	4.246	0.120	0.297	5.769	0.110	0.197
^{19}F	4.377	0.656	0.823	10.033	0.871	3.055	10.620	1.634	4.248
^{23}Na	4.735	0.472	0.563	6.914	0.351	1.746	9.465	1.369	4.123
^{24}Mg	5.107	0.585	0.975	1.964	0.583	0.657	0.047	0.452	0.945
^{25}Mg	8.868	1.809	2.938	7.050	0.440	2.076	4.081	0.228	0.417
^{26}Mg	4.219	0.985	1.698	2.916	0.472	0.563	6.046	0.844	1.014
^{27}Al	5.501	0.031	0.972	6.707	0.585	0.975	9.361	1.779	4.617
^{28}Si	6.249	1.273	2.028	1.427	0.228	0.417	0.523	1.384	1.954
^{29}Si	8.385	2.235	3.499	6.012	0.844	1.014	3.375	0.677	0.709
^{30}Si	4.364	1.249	2.235	3.127	0.031	0.972	5.072	1.266	2.234
^{31}P	5.712	0.078	0.513	8.165	1.273	2.028	6.640	2.230	3.778
^{32}S	6.418	0.841	1.966	4.900	0.677	0.709	0.052	0.811	1.987
^{33}S	9.192	2.127	3.303	8.565	1.266	2.234	2.917	0.146	0.461
^{34}S	4.762	1.572	1.991	5.084	0.078	0.513	4.147	1.219	1.763
^{36}S	2.071	0.645	1.400	4.592	0.429	1.608	6.160	1.727	3.087
^{35}Cl	6.355	0.788	1.165	8.283	0.841	1.966	6.282	1.970	4.178
^{37}Cl	3.883	0.671	0.755	7.795	1.572	1.991	8.018	2.168	3.377

*These states of the final nucleus are unbound and can decay with emission of particles.

here one must take into account the background intensity, which also depends on the energy. For thicker targets, the yield curves depend on the depth distribution $N_A(x)$, and therefore information about the depth distribution can be obtained from the spectra and the yield curves. In accordance with Eqs. (5) and (10), the radiation energies and the intensities depend on the Q value of the reaction, the level schemes, and the reaction cross sections. A general theoretical description of all these quantities is not possible, and for analytic purposes one can use only experimental information. For nuclei with charge up to $Z = 21$, the corresponding materials are given or cited in the reviews of Refs. 16 and 17, and in Refs. 18–22 and 23.

Data on the energy-dependent cross sections or yield curves for light nuclei are collected together in Refs. 24 and 25. A general survey of the corresponding references on measurements of the cross sections and yields is given in Ref. 26.

For proton- and deuteron-induced reactions with target nuclei up to ^{37}Cl the Q_0 values of the ground states and the excitation energies for the two lowest-lying states of the final nuclei are given in Tables I and II. We have included here primary γ rays in proton-capture reactions, and also protons, neutrons, and α particles as emitted objects.

3. ANALYSIS OF SURFACE REGIONS IN SOLIDS

1. General aspects

Analysis of surface regions by means of resonance nuclear reactions can be widely applied. The range of applications extends from analysis of traces of elements in contamination on a surface or in the region of small depths to the determination of stoichiometric ratios of thin layers to thick substrates. Included here are measurements of the total concentration or the distribution with respect to the depth of a number of isotopes in the surface region. In addition, nuclear reactions are frequently used to determine the changes in the impurity concentration and the depth profiles as functions of the method of formation purification, and treatment.

Finally, final charged particles with depth-dependent energies $E(x)$ and secondary γ rays with constant energies E corresponding to the spacings between the levels of a produced nucleus are used for purposes of analysis. The main stages of this work are as follows:

i) The energy spectra for fixed energy E_0 of the incident ions are specified. The spectra of the charged particles may give an incomplete picture about the depth distribution $N_A(x)$, whereas the individual spectra of the secondary γ rays give no information at all about the depth, since their energy E_γ does not depend on the depth.

ii) The reaction yields are measured as functions of the incident-particle energy E_0 for a number of radiation components. This method is well suited to the determination of depth profiles and ensures narrow and isolated resonances for the reaction cross section. Also helpful are the yield functions for particles and γ rays.

In both methods, important characteristics are the attainable detection limit and the resolution depth. In many cases, detection limits significantly lower than a monolayer

have been achieved. However, it is difficult to make generalizations because of the influence of the material substrate itself.

The depth resolution $\delta t(x)$ at depth x can be characterized for both methods of analysis as

$$\delta t(x) = \frac{\delta E(x)}{dE/dx}. \tag{13}$$

Here, the energy resolution $\delta E(x)$ is given by the half-width of the peak in the spectrum or the yield curve measured under conditions when the nuclei A are contained in the target only in a very thin layer at depth x. This energy-resolution function includes the system resolution δE_{sr} and the energy-dependent component $\delta E_{st}(x)$ of the spread with respect to the energy (straggling) E. Using the Gaussian approximation, these terms give the quadrature

$$\{\delta E(x)\}^2 = \{(\delta E_{sr})\}^2 + \{(\delta E_{st}(x)\}^2. \tag{14}$$

Both the system resolution and the straggling component depend on the method that is used. Here, dE/dx describes the specific energy loss by charged particles (incident and final particles) in the matter of the target. To obtain a good depth resolution through a large value of dE/dx, it is best to use heavy particles.

Which of the procedures described above is best suited for a particular analysis depends on the behavior of the cross section in the chosen region, on the depth resolution, and on the required sensitivity. It is necessary to take into account questions related to the background and competing processes, like interference and superimposed radiations due to other reactions.

In Secs. 3.2–3.5, we attempt to survey the different fields of application of the listed methods of investigation. We consider several examples for both methods of measurement and discuss the application of these methods in connection with particular problems of analysis. Many other examples, together with details of different investigations, can be found in the proceedings of conferences on the use of ion beams for purposes of analysis[27–33] and in the cited references, respectively.

2. Narrow resonances

In proton-induced reactions, narrow and isolated resonances are often observed (see Fig. 6). In the region of such a resonance, the total cross section $\sigma(E)$, defined as

$$\sigma(E) = 2\pi \int_0^\pi \sigma(\theta, E) \sin\theta \, d\theta, \tag{15}$$

is described by the Breit–Wigner formula, which can be represented in the form

$$\sigma(E) = \sigma_m \frac{(\Gamma/2)^2}{(E - E_r)^2 + (\Gamma/2)^2}. \tag{16}$$

Here, σ_m and Γ are the maximal cross section for the resonance energy E_r and the total width of the resonance, respectively. These resonances and the corresponding parameters of the resonances are characteristic for unbound states of the compound nuclei and can be used for their identification. Therefore, for known incident particles, these resonances serve for identification of the corresponding target nuclei A; σ_m depends on the reaction channel and is the sum of all the partial widths Γ that are characteristic of the different forms of decay of the compound state.[14] The total cross section $\sigma(E)$ is measured in barns, whereas the partial cross section $\sigma(\theta, E)$ is usually expressed in barns per steradian. For $\sigma(\theta, E)$, one must take into account the angle-dependence factor. We denote this by $\sigma_m = \sigma_m(\theta)$. Particularly striking angular dependences $\sigma(\theta, E)$ have been observed in the case of particle emissions. For γ rays one frequently finds a weak angular dependence.

These narrow and isolated resonances are well suited for the determination of the depth profiles. Near resonance, one observes large radiation yields. In accordance with Eq. (16), these yields decrease to $0.01\sigma_m$ at a distance $|E - E_r| \approx 5\Gamma$ from the resonance.

Within the target, the incident particles are decelerated. Incident particles with energy $E_0 > E$ acquire a resonance energy in the region of the depth x_0. Because of the strong energy dependence of the cross section, the yield $Y(\theta, E_0)$ is roughly proportional to $N_A(x_0)$, and the yield curve $Y(\theta, E_0)$ gives an idea of the depth distribution $N_A(x)$.

Under real conditions, the energy-straggling effects lead immediately to a deterioration of the depth resolution. Taking into account the real energy distribution $n(E_0, \bar{E}_0)dE_0$ of the beam and the straggling, which are ignored in Eqs. (11) and (12), we can write the exact relationship between $Y(\theta, E_0)$ and $N_A(x)$ in the form

$$Y(\theta, \bar{E}_0) = \varepsilon \int \left\{ \int \left[\int n(\bar{E}_0, E_0) W(E_0, E, x)\, dE_0 \right] \sigma(\theta, E)\, dE \right\} N_A(x)\, dx. \tag{17}$$

Here, $\bar{E}_0$ is the mean energy of the incident particles, and $W(E_0, E, x)$ describes the probability that a particle with bombarding energy E_0 on the surface has energy of order E at depth x. The determination of the depth profile requires unfolding of the measured yield function. However, more qualitative information can be obtained directly from the measurements of the yield curves.

When the yield functions are used, the energy resolution is characterized by the half-width $\delta\bar{E}_0(x)$ of the measured resonance peak. Contributions to the system resolution are made by the energy spread of the incident particles, the total resonance width Γ, and the Doppler effect δE_D on the effective reaction energy. As was shown in Ref. 38, this last term, due to the Doppler effect, need be taken into account only in the case of very narrow resonances.

The yield functions measured by means of different particles and γ rays are expressed as corresponding to definite radiation components. Therefore, only the energy spread of the incident particles contributes to the energy resolution, which can be represented as

$$\{\delta\bar{E}_0(x)\}^2 = \Gamma^2 + (\delta E_0)^2 + (\delta E_D)^2 + (\delta E_{st}^a(x))^2. \tag{18}$$

Here, $\delta\bar{E}_0(x)$ does not depend on the detector resolution and the additional absorbers used to suppress the scattered ions. To determine the depth resolution in accordance with Eq. (13), we must take into account the specific energy loss $dE/dx = NS_a(E_r)$ taken at the resonance energy of the incident particles.

The system resolution can be measured experimentally by measuring the yield curve for a very thin target. A good system resolution is possible if the resonance width Γ and the energy spread δE_0 of the beam are small.

3. Use of yield functions

Resonance reactions induced by protons are widely used for the detection and determination of fluorine depth profiles. Large yields are obtained in the $^{19}F(p, \alpha\gamma)^{16}O$ and $^{19}F(p, p\gamma)^{19}F$ reactions, which lead to the emission of high-energy ($E_\gamma = 6.13 \ldots 7.15$ MeV) and low-energy γ rays, respectively. The yields of both reactions for thin targets are given in Ref. 34, while Ref. 35 contains data on the yields of the $(p, \alpha\gamma)$ and (p, α_0) reactions for thin targets. The yield curves were measured simultaneously in Ref. 36 for thin targets for γ-ray transitions in both of these processes. These results are shown in Fig. 6. In addition, data on the parameters of the resonances are given in Ref. 22. For the detection of high-energy γ rays from the $^{19}F(p, \alpha\gamma)^{16}O$ reaction, many authors have used a large-volume NaI detector. All events within the wide energy window $E_\gamma \approx 3$–7.5 MeV were detected as a ^{19}F signal. The resonance with energy $E_r = 1371$ keV ($\Gamma \approx 12$ keV) was used in Ref. 37 to determine fluorine on the surface of zircalloy and below it after different manipulations.[37] It was found that unoxidized samples contain fluorine on the surface and in surface layers thinner than 0.1 μm, whereas in oxidized samples ^{19}F nuclei are distributed to a depth of a few microns. The sensitivity was estimated at $\lesssim 0.01$ mg of fluorine per 1 cm^2.

Fluorine depth profiles near a Ta_2O_5–Ta surface have been reported in Refs. 38 and 35. Fluorine to about 1.6×10^{15} F atom/cm^2 was deposited on a tantalum surface by a special treatment. These samples were anodized in order to obtain Ta_2O_5 layers of thickness 76 and 156 nm. In both cases—for the oxidized and unoxidized substrates—the yield curves of the $^{19}F(p, \alpha\gamma)$ reaction were measured in the region of the resonance energies $E_r = 872$ keV ($\Gamma \approx 4.5$ keV) and $E_r = 340$ keV ($\Gamma \approx 2.4$ keV). The results are given in Fig. 9. For energy $E_r = 872$ keV only the yield curves obtained for the contaminated Ta surface and for the thicker oxidized layer (156 nm) are given, while for the energy $E_r = 340$ keV the results for the thick 76-nm Ta_2O_5 layer are also included. The continuous curves correspond to calculations made under the assumption that the fluorine atoms are concentrated in a thin layer (50 nm) at the metal-oxidized surface. A better depth resolution and lower counting rate can be clearly seen for $E_r = 340$ keV. But the yield is still acceptable for determination of the fluorine concentration at a depth that is equivalent to about two monolayers.

In Ref. 39 a study was made of layered foils of iron with fluorine implanted in layers with 2×10^{16} and 2×10^{17} F atoms/cm^2. Using resonances E_r equal to 340 and 484 keV ($\Gamma = 0.9$ keV), the authors observed fluorine diffusion after heating to $T = 100$–450 °C. Above the temperature 450 °C instantaneous oxidation was observed; this led to migration of the fluorine, which was then observed immediately below the oxide layer. A high sensitivity and low background were obtained for $E_r = 340$ keV, and this permitted depth profiling down to 250 nm.

Other applications of the $^{19}F(p, \alpha\gamma)^{16}O$ reaction are to the determination of fluorine in tooth enamel,[34,35] in samples of lunar soil,[41] and in the use of nuclear microprobes in archeological and geological materials.[42]

In the case of a matrix of heavy elements, it is preferable to use a large-volume NaI detector in conjunction with a wide energy window for γ rays. This means that the γ background due to the reaction on the substrate is small within the chosen range of γ rays. This condition can be made more stringent for light target materials such as Al, Si, and Na, which use high-energy captured γ rays. In these cases, the $^{19}F(p, p'\gamma)^{19}F$ reaction, which leads to the appearance of lines with E_γ equal to 110 and 197 keV, permits not only the detection of ^{19}F but also the determination of its depth profile. Of course, one must use Ge(Li) detectors with high resolution, but in many cases the γ background is large for these low-energy photons. However, one can subtract the background from the narrow γ peak and determine its true intensity. By means of a minicomputer the background-separation procedure can be carried out automatically. In this manner, the γ-ray yield curves given in Fig. 6 were obtained. In Ref. 43, the $^{19}F(p, p'\gamma)^{19}F$ reaction was used to measure fluorine impurities in different materials. After etching by fluoric acid to eliminate a layer of natural oxide from substrates of pure silicon a residual fluorine contamination of 5×10^{13} F atoms/cm^2 was observed despite extensive purification and rinsing. Without etching by the fluoric acid, fluorine impurities were not found. These measurements were made on the basis of the strong resonance $E_r = 933.6$ keV ($E_\gamma = 110$ keV, $\Gamma = 8$ keV), and the surface contamination were measured at the maximum of the resonance.

In Ref. 44, the $^{19}F(p, p'\gamma)^{19}F$ reaction was used to analyze fluorine in thick samples of food products. Protons with energies $E_p = 2.8 \ldots 3.5$ MeV were used, and for high ^{19}F

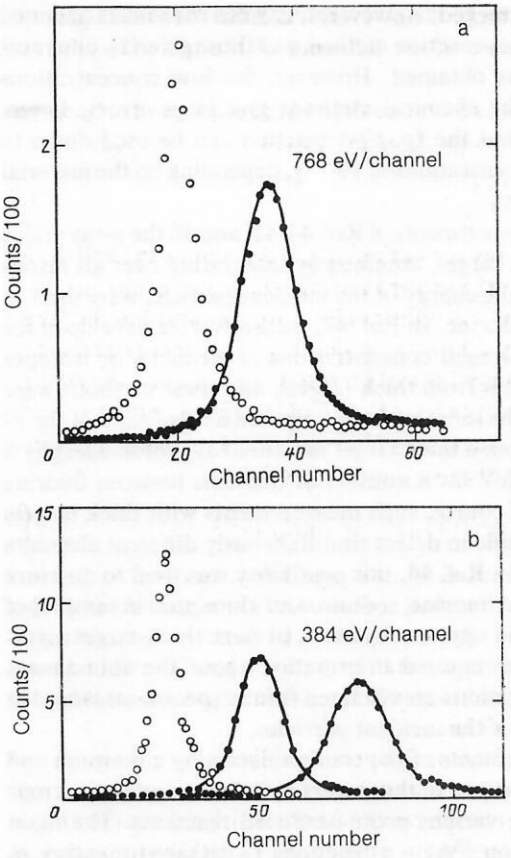

FIG. 9. Depth profiles of fluorine in a tantalum sample. The fluorine contaminated the sample as a result of a treatment with fluoric acid. The measurements were made before and after anodizing: a) $E_r = 8.72$ keV, oxide film of thickness 156 nm; b) $E_r = 340$ keV, oxide films of 76 and 156 nm, respectively (figure taken from Ref. 38).

concentrations good agreement between the results obtained by the nuclear-reaction method and those given by chemical methods was obtained. However, for low concentrations ($< 10^5$ g) the chemical methods give large errors. It was concluded that the $(p, p'\gamma)$ reaction can be used down to fluorine concentrations of 10^{-7} g, depending on the material of the matrix.

In the experiments of Ref. 44, 45, and 46 the γ-ray yields from a thick target, obtained by integrating over all resonances up to the energy of the incident particle, were used to determine fluorine. In Ref. 47, methods were developed for deducing averaged concentrations of elements or isotopes from the yields from thick targets, and these methods were discussed. The same authors proposed a tabulation of the γ-ray yields from a thick target measured at proton energies 2 and 2.514 MeV for a number of elements between fluorine and gold. Of course, such measurements with thick targets make it possible to detect simultaneously different elements or isotopes. In Ref. 46, this possibility was used to measure the amount of fluorine, sodium, and aluminum in samples of black volcanic vitreous obsidian. In these thick-target investigations, the required information about the abundances and concentrations are obtained from γ spectra measured at fixed energy of the incident particles.

Measurements of the contamination by aluminum and the concentrations in thin layers have been made by various groups using various proton-induced reactions. The main information on $^{27}\mathrm{Al} + p$ reactions is gathered together in Ref. 23. The thick-target yield function for the $(p, p'\gamma)$, $(p, \alpha\gamma)$, and (p, γ) processes, which lead to γ rays with energies E_γ equal to 843 and 1013, 1368, and 1778 keV, respectively, were measured in Ref. 48. The corresponding yield curves for thin targets are given in Ref. 49.

The amounts of α-aluminum and magnesium, which are used as polishing substances (mean grain size 0.3 and 1 μm, respectively), remaining in metals of different hardness after a standard polishing and washing procedure were investigated in Ref. 50. The $E_r = 992$ keV resonance of the $^{27}\mathrm{Al}(p, \gamma)^{28}\mathrm{Si}$ reaction was used. Only high-energy primary γ rays, leading to the appearance of the first excited state of ^{28}Si with energy 1.778 MeV, were counted by means of a 3×3 inch NaI detector. The yield curves obtained for Zr, Au, and Cu targets are given in Fig. 10. For Zr (upper curve) the yield function corresponds to particles with diameter 0.3 μm localized on the surface. The Al surface density, equal to 0.15 mg/cm^2, was obtained from the area of the resonance. The polishing compounds were retained to a greater degree in the gold target, as indicated by the large area of the peak. The peak is broadened by the fact that some particles are disseminated in the gold. Finally, there are even more particles of the polishing compounds in the copper, and they are disseminated more deeply. An appreciable fraction of them is situated at depth 1 μm and is covered by copper (lower curve). These investigations provide an example in which the resolution of the system ($\Gamma = 100$ eV, $\delta E_0 \approx 1$ keV) make it possible to ignore in practice the effects of the energy spread.

Similar measurements were made for powdered magnesium using the resonance with energy 1.548 MeV of the $^{26}\mathrm{Mg}(p, \gamma)]^{27}\mathrm{Al}$ reaction.

The resonance with energy 992 keV ($\Gamma = 100$ eV) was also used in Refs. 5 and 38 to investigate an Al_2O_3 film of thickness 47.5 nm on an aluminum layer of thickness 0.8 μm. All γ rays in the interval $E_\gamma = 1.3$–13 MeV were detected by means of a 3×3 inch NaI detector. The measured yield function is shown in Fig. 11. Using a proton beam with a small energy spread, the authors obtained an energy resolution of about 300 eV; this corresponds to a 6-nm depth resolution at the surface of the target. The abrupt jump at the resonance energy and the clearly expressed plateau indicate the good resolution. The slow rise at a somewhat higher proton energy is due to the energy spread in the oxide film and characterizes the capacity of the resonance protons to penetrate into the aluminum layer. The step heights Δ_1 and Δ_2 (Fig. 11) depend on the Al atomic density and the stopping cross sections of both materials, and the stochiometric ratio is determined as

$$\frac{N_{\mathrm{Al}}}{N_0} = \frac{\Delta_1/\Delta_2}{1-(\Delta_1/\Delta_2)} \frac{S_0(E_r)}{S_{\mathrm{Al}}(E_r)}. \qquad (19)$$

It is here assumed that in the thin oxide layer the total resonance integral contributes to the measured plateau yield. The stochiometry of such thin layers can be determined only if a good energy resolution has been obtained. In Refs. 5 and 38 it could be shown in this way that the stochiometric composition does indeed represent Al_2O_3.

In the majority of applications of resonance reactions to

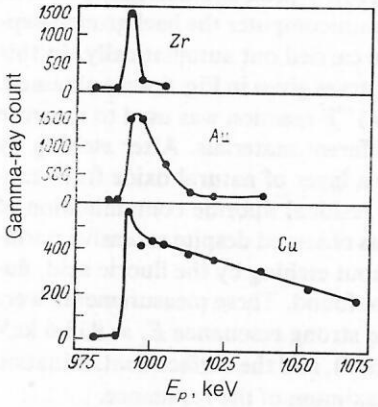

FIG. 10. Yield curves of the $^{27}\mathrm{Al}(p, \gamma)^{28}\mathrm{Si}$ reaction measured on a polishing Al_2O_3 compound remaining on the surface of Zr, Au, and Cu (figure taken from Ref. 50).

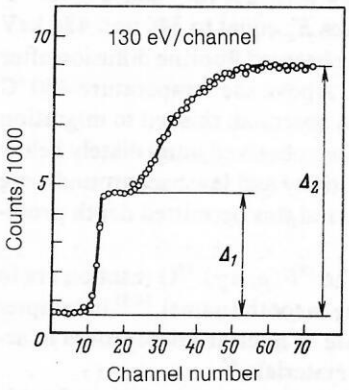

FIG. 11. Yield function of the $^{27}\mathrm{Al}(p, \gamma)^{28}\mathrm{Si}$ reaction near the resonance with energy 992 keV obtained for an aluminum target covered with an Al_2O_3 film of thickness 47.5 nm (figure taken from Ref. 5).

determine depth profiles the emitted γ rays are used to identify isotopes. This is possible because of the strong contribution of the backscattered incident particles to the spectrum of the emitted particles. The scattering cross section is usually orders of magnitude greater than the nuclear-reaction cross sections. Therefore, the beam current must be reduced to prevent the backscattered ions from blocking the amplifier, or the backscattered incident particles are suppressed by additional absorbers placed in front of the particle detector. A different procedure was used in Ref. 56—a 180° double focusing magnetic spectrometer was used to select the scattered particles. The Al concentration was measured as a function of the depth in epitaxially grown films of silicon on a sapphire matrix. These investigations used the resonance with energy $E_p = 1365$ keV ($\gamma = 1.1$ keV) of the $^{27}Al(p, \alpha)^{24}Mg$ reaction.

Thin films of GaAs and GaAlAs oxides grown in a plasma were analyzed in Ref. 57 by the combined methods of Rutherford backward scattering, ion-induced x-ray emission, and profile determination by means of nuclear resonances. The Al depth profiles were found by means of the $^{27}Al(p,\gamma)^{28}Si$ reaction in the region of the resonance with $E_r = 992$ keV.

Most chemical elements consist of a mixture of isotopes. For example, natural oxygen and nitrogen contain 0.204% of ^{18}O and 0.365% of ^{15}N, respectively. In Ref. 5, ^{18}O was used as a tag in a study of oxygen transport in the process of tantalum anodizing. The $^{18}O(p, \alpha)^{15}N$ resonance reaction in the region of the resonance 629 keV ($\Gamma = 2.5$ keV at 165°) was used to measure the ^{18}O depth profiles for special Ta samples anodized in ^{18}O-enriched or natural water. The yield curves clearly confirmed that oxidation in tagged solutions leads to the appearance of ^{18}O-tagged oxide films. The detailed analysis showed that the mixture of tagged and untagged layers in the films extended only to a few hundred parameters. The depth resolution in Ta_2O_5 was estimated at 20 nm.

In Ref. 38, sandwich targets consisting of ^{18}O-enriched and natural Ta_2O_5 layers were studied by means of the $^{18}O(p, \alpha)^{15}N$ and $^{18}O(p, \gamma)^{19}F$ reactions. In the latter case, the particularly narrow resonance with energy $E_p = 1167$ keV ($\Gamma \approx 5$ eV) was used. When allowance was made for all the effects of the energy spread, the yield functions, which were measured using a beam with a very small energy spread, could be excellently reproduced by means of model calculations. Very thin oxide films as well as deep ^{18}O-enriched Ta_2O_5 layers were studied. The results showed that small film thicknesses could be determined with high accuracy.

Resonance scattering of α particles can also be used to determine the amount of oxygen and the depth profiles. As was shown in Ref. 51, there exists a strong $^{16}O(\alpha, \alpha)^{16}O$ resonance with energy $E_\alpha = 3.036$ MeV and $\Gamma_{cms} = 8.1$ keV.[22] The cross section of the resonance, $\sigma_r = 0.95 \times 10^{-24}$ cm^2, is approximately 25 times greater than the extrapolated Rutherford cross section. The resonance exhibits a very strong dependence on the detection angle.

In Ref. 52, this resonance was used to determine oxygen in thin metallic films and thick silicon matrices. Enhanced oxidation of silicon after implantation of antimony in this material was found.

In Ref. 53, the same resonance was used to measure the oxygen concentration on a silicon surface as well as in thin gold (34 nm) and gold (34 nm) plus germanium (10 nm) films on a thick silicon matrix. For the gold and gold–silicon films total oxygen concentrations of 1×10^{16} and 1.6×10^{16} atom/cm^2, respectively, were found.

In Ref. 54 metal–semiconductor junctions were studied by various methods. Mass spectroscopy of secondary ions and the $^{16}O(\alpha, \alpha)^{16}O$ reaction were used in an investigation of the accumulation of oxygen at a gold–silicon interface. The depth scale for the results obtained by the mass spectroscopy of the secondary ions was calibrated by means of the Rutherford backward-scattering method using backward scattering of $^4He^+$ with energy 1 MeV.

Porous materials were investigated in Ref. 55 by means of the $^{16}O(\alpha, \alpha)^{16}O$ resonance described above and also the $^{16}O(p, p)^{16}O$ scattering resonance with energy $E_p = 2.66$ MeV ($\theta = 170°$). Comparing the measured widths of the resonances for porous and nonporous aluminum oxide, the authors estimated the mean pore size. The method was used to study pores with mean diameter from 0.1 to 100 μm.

Some other possibilities for detecting and determining oxygen depth profiles on the basis of charged-particle spectra are given in subsection 5 of this section.

Nuclear reactions are an excellent tool for detecting hydrogen and determining its depth profiles. The probability that a nuclear reaction takes place between colliding particles ($a + A$) depends on their relative kinetic energy, i.e., on the energy in the center-of-mass system. On the replacement of particle a by a target nucleus, the resonance observed at energy E_r^a (when the light particle is used as a bombarding ion) is excited at energy E_r^A,

$$E_r^A = \frac{m_A}{m_a} E_r^a, \tag{20}$$

and the heavier nucleus A with mass m_A plays the role of incident particle.

In Ref. 58, hydrogen depth profiles in lunar soil samples were determined using the $^1H(^{19}F, \alpha\gamma)^{16}O$ reaction in the energy interval $E_F = 16$–18 MeV. The resonance at $E_F = 16.44$ MeV corresponds to the $^{19}F(p, \alpha\gamma)^{16}O$ resonance at $E_p = 872$ keV ($\Gamma = 4.7$ keV). For the incident ^{19}F atoms the width of the resonance in the laboratory system is $\Gamma \approx 90$ keV, since the widths are transformed in the same way as the resonance energies. In this connection, it should be noted that the Breit–Wigner formula [see Eq. (16)] is valid in the center-of-mass system and describes the cross section in both of the cases considered here.

In Ref. 59, different methods using an ion beam to determine hydrogen profiles were compared, and nine of these methods were tested for similar silicon samples with hydrogen ions implanted in them. The analytic possibilities extend from a very high depth resolution (≈ 5 nm) and high sensitivity ($< 10^{-6}$ g) to hydrogen probing to a depth of 0.2 mm. In what follows, we shall limit ourselves to just some of the applications of the resonance reactions.

In accordance with Eq. (13), good depth resolution for the hydrogen profiles can be achieved because of the large stopping cross section for the heavier incident particles.[15] However, in the laboratory system the widths of the resonances are much greater. Therefore, to obtain a particularly good depth resolution appropriately narrow resonances are required. On the other hand, the energy spread of the beam

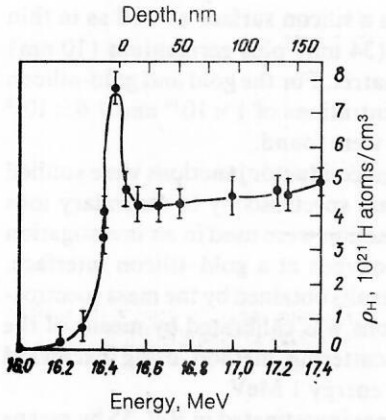

FIG. 12. Hydrogen depth profile in electrically deposited solid gold obtained by means of the resonance nuclear reaction $^1H(^{19}F, \alpha\gamma)^{16}O$ (figure taken from Ref. 60).

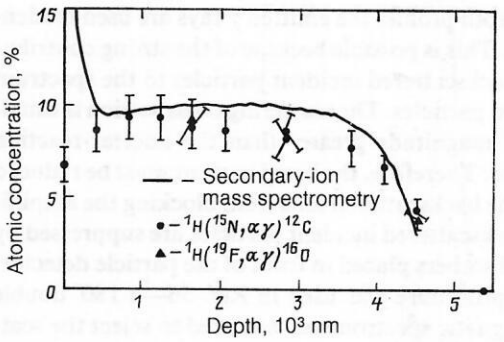

FIG. 13. Hydrogen depth profiles in amorphous silicon measured by means of nuclear reactions and secondary-ion mass spectroscopy (figure taken from Ref. 60).

plays a smaller part because of the relatively large widths of the resonances in the laboratory system.

Although hydrogen has a high mobility in the majority of materials, a careful choice of the irradiation conditions is an important prerequisite if hydrogen is not to be lost during the time of the measurements. If this is impossible, then the hydrogen signals must be measured over a period as a function of the accumulated ion charge and the yield extrapolated to the beginning of the irradiation process.

In Ref. 60, the $^1H(^{19}F, \alpha\gamma)^{16}O$ and $^1H(^{15}N, \alpha\gamma)^{12}C$ reactions were used to analyze hydrogen in the fields of metallurgy, mineralogy, and semiconductor technology. A special investigation was made with hydrogen inclusions in electrodeposited gold. An atomic concentration of hydrogen in the interval from 0.26 to 9% was established by using various chemical baths and a temperature regime. High-energy γ rays were detected by means of a 3×3 inch NaI detector. As an example, Fig. 12 shows the yield curve measured near the resonance of the $^1H(^{19}F, \alpha\gamma)^{16}O$ reaction with energy 16.44 MeV. A strong hydrogen peak from the surface and a roughly constant ^1H admixture in the gold layer is observed. Natural and synthetic quartz were also investigated, and in all cases contamination of the surface by hydrogen was found, together with a broad region below the surface with thickness of about 200 nm with a relatively high hydrogen concentration and a deeper region in the material from which the γ-ray yield was small. Before the investigation, these samples were covered by a thin graphite film (12 mg/cm^2) to avoid accumulation of charge. The authors also made such measurements on deposited electroluminescent amorphous silicon films. Hydrogen inclusions were studied by means of resonance reactions and mass spectroscopy of secondary ions. To permit direct comparison of the different methods, the same films were used. The result of the comparison are shown in Fig. 13 and reveal a good agreement for the different methods. The amount of hydrogen in the film was found to be 9%.

Later, Clark and his collaborators compared the analytic possibilities of the resonances with energy 16.44 MeV ($\Gamma\approx90$ keV) and 6.385 MeV of the $^1H(^{19}F, \alpha\gamma)^{16}O$ and $^1H(^{15}N, \alpha\gamma)^{12}C$ reactions, respectively. The main advantage of the 16.44-MeV resonance is its higher yield for given integrated beam charge and, therefore, higher sensitivity. On the other hand, the smaller width of the 6.385-MeV resonance gives a better depth resolution and leads to clearer identification of the peak of the surface hydrogen. For the half-width of this resonance different values have been given in the literature.[21,61] The detailed analysis of the resonance in

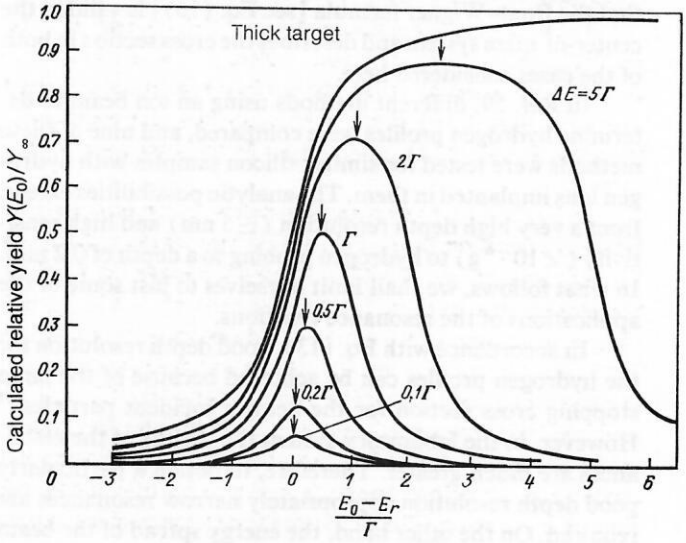

FIG. 14. Shape of resonance calculated as a function of the energy loss ΔE in the target. All the other effects of energy spreading are ignored.

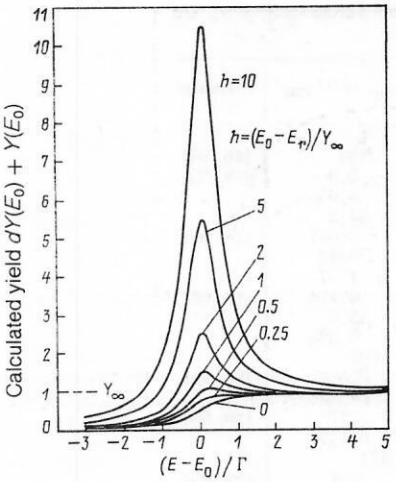

FIG. 15. Yield function calculated for constant concentration in the interior of the sample and different surface contaminations. The intensity of the surface peak is normalized to the total yield Y_∞ given by the complete volume of the material. The ordinate is measured in units of Y_∞.

Ref. 61 showed that the half-width $\Gamma \approx 6$ keV contradicts the value $\Gamma = 15$ keV obtained and measured by Clark and collaborators. In Ref. 61, the large experimental half-width is attributed to effects of the target thickness.

As was demonstrated in Fig. 14 by means of simple model calculations which ignore all effects of energy spreading except the target thickness x, the energy loss ΔE in a target of finite thickness leads to deviations of the shape of the measured resonances from the Lorentz distribution in Eq. (16). Further, one observes a shift of the resonance equal to $\Delta E/2$. The curves in Fig. 14 were calculated for mean energy losses $\Delta E = 0.1\Gamma \ldots .5\Gamma$, and also for an infinitely extended target. The arrows indicate the positions of the peaks.

Figure 15 gives the results of calculations using an analytic model; they illustrate the superposition of the yield functions for a constant contamination N_H^{vol} (atom/cm^3) of the complete volume and a surface contamination $(N_H dx)^{surf}$ (atom/cm^2) with variable surface density. The energy loss in the surface layer was ignored, and the intensity h of the surface peak was expressed in units of the yield Y_∞ from a thick target for the complete volume of the material. The connection between the two types of contamination,

$$(N_H dx)^{surf}/\cos\theta_1 = h\left(\frac{N_H}{N_M S_M(E_r)}\right)^{vol}\frac{\pi}{2}\Gamma, \qquad (21)$$

depends on the resonance width Γ and on the total volume of the material. A surface peak is clearly seen for $h \gtrsim 1$. In the case of large resonance widths Γ and high concentrations N_H^{vol} in the complete volume, the surface contamination can be manifested only in a shift of the step of the function for the thick target (see Fig. 15 for $h \lesssim 1$).

Systematic investigations of the hydrogen surface peak were made in Ref. 62 by means of the ^{2}H(^{11}B, $\alpha)\alpha\alpha$ resonance reaction. For different vacuum conditions and materials, the peak intensity was measured as a function of the irradiation exposure. In Ref. 63 the hydrogen concentration and the density of amorphous $Si_{1-x}C_xH_z$ and SiH_z films were studied using backward Rutherford scattering, infrared spectroscopy, and the ^{1}H(^{11}B, $\alpha)\alpha\alpha$ reaction. A

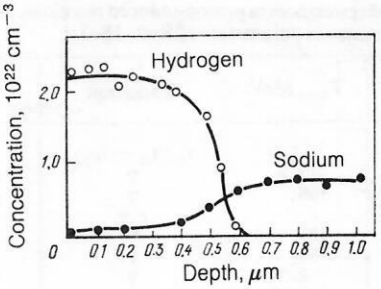

FIG. 16. Profiles of hydrogen and sodium concentrations in the surface layer of a hydrated glass sample (figure taken from Ref. 61).

strong influence of the amount of hydrogen on the density of the $Si_{0.5}C_{0.5}H_z$ layers was found. Further, the decrease of the hydrogen concentration as a function of the bombardment by the ion beam was studied for $Si_{1-x}C_xH_z$ films. Whereas for small values of x or z a constant hydrogen concentration was observed, it changed for large x or z from the given initial value to an equilibrium value which could be much less than the original value. Using infrared measurements, the authors interpreted this result as transfer of hydrogen from CH_n to SiH_1 centers. For $x = 0$ and ^{11}B bombardment, hydrogen liberation was not found.

In Ref. 61, the method of determining hydrogen profiles by means of ^{15}N was used to investigate processes of glass hydration and to study the influence of hydrogen in superconducting Nb_3Ge on the transition temperature. Glass samples were first etched to avoid any surface hydration and were then hydrated in a thermal bath with distilled water. The ^{1}H(^{15}N, $\alpha\gamma)^{12}$C resonance with energy 6.385 MeV ($\Gamma \approx 6$ keV) was used to measure hydrogen profiles for samples hydrated at 90° for about 500 h. From the dependence of the thickness of the hydrated layers on the hydration time it can be seen that the thickness increases as the square root of the time and then appears to become constant. The ^{23}Na(p, $\gamma)^{24}$Mg reaction was also used to measure the sodium depth profile. Figure 16 compares the measured hydrogen and sodium profiles. The results show that during the hydration process Na ions are replaced by hydrogen-bearing ions. The ratio of the maximal hydrogen concentration to the maximal sodium concentration is 2.9 ± 0.3. Therefore, approximately three ^{1}H atoms participate in the replacement of a sodium atom or ion.

In the analogous investigations of Ref. 64, the ^{1}H(^{15}N, $\alpha\gamma)^{12}$C, ^{23}Na(p, $\alpha\gamma)^{20}$Ne, and ^{27}Al(p, $\gamma)^{28}$Si resonance reactions were used to study the surface regions of different glasses. It was shown that certain elements, like aluminum, have the ability to retard appreciably the hydration of the glasses.

In Ref. 65, hydrogen and fluorine were determined in a SiO_2/Si transition layer. Films of silicon oxide grown in a Cl_2/O_2 medium at 1100 °C for 15 min were studied. Cooling the targets to a final steady temperature of -130 °C and using a beam current 8 nA or less and a beam spot measuring 2×2 mm, the authors measured the hydrogen profile near the surface of the junction by means of the ^{1}H(^{19}F, $\alpha\gamma)^{16}$O reaction. They suggested that the failures of the experiment could be mainly due to the fact that the samples were not cooled and, therefore, the hydrogen was mobile during the time of irradiation. The measured hydrogen profiles agreed

TABLE III. Some recommended resonances in proton-induced reactions. The resonance integrals I_r and maximal cross sections σ_m are calculated on the basis of the resonance parameters of Refs. 18–23.

Target nucleus	E_r, MeV	Γ_{lab}, MeV	Radiation	E_b [a], MeV	I_r, 10^{-24} cm^2·eV	σ_m, 10^{-27} cm^2	References
^{6}Li	1.85 [b]	≈ 500	$\alpha_0\,(R_\alpha < R_p)$	1.443	$1.44\cdot10^5$	184	[18, 94]
^{7}Li	0.441	12.2	γ	≥ 17.641	113.6	5.9	[18, 95]
	1.03	168	γ	≥ 18.156	13.2	0.05	
			$p_1\gamma$	0.478	$1.17\cdot10^3$	44.3	
^{9}Be	0.320	133	γ	≥ 6.873	8.5	0.041	[18, 95]
	0.992	80	γ	≥ 7.477	53.4	0.43	
	1.083	2.94	γ	≥ 7.560	5.0	1.07	
^{11}B	0.163	5.67	γ	≥ 16.107	1.55	0.174	[19, 95]
			$\alpha_1\,(R_\alpha > R_p)$	3.668	405	45.5	
	0.675 [c]	327	γ	≥ 16.58	17.4	0.034	
			$\alpha_1\,(R_\alpha > R_p)$	3.732	$3.1\cdot10^5$	604	
^{12}C	0.459 [d]	36.5	γ	2.365	4.7	0.082	[20, 95]
	1.699 [d]	67.6	γ	3.511	3.6	0.034	
^{13}C	0.511	32.5	γ	≥ 8.062	59.4	1.17	[20, 95]
	1.462	17.3	γ	≥ 8.907	4.06	0.147	
	1.748	0.076	γ	≥ 9.172	50.3	421	
^{15}N	0.338	96	γ	≥ 12.444	1.55	0.01	[21, 95]
			$\alpha_0\,(R_\alpha > R_p)$	3.714	12 300	81.5	
			$\alpha_1\gamma$	4.430	3.24	0.021	
	0.429 [c]	0.9/0.4	$\alpha_1\gamma$	4.430	272	192/432	[61]
	0.897 [c]	2.0	$\alpha_1\gamma$	4.430	2687	856	
	1.028	140	γ	≥ 13.091	77.7	1.55	
			α_0	4.021	97 114	442	
	1.210	22.5	$\alpha_1\gamma$	4.430	10 042	284	
	1.640	68	γ	≥ 13.664	2.7	0.025	
			$\alpha_1\gamma$	4.430	18 481	173	
^{18}O	0.633	2.1	$\alpha_0\,(R_\alpha > R_p)$	3.343	893	271	[22, 95]
	0.987	3.8	α_0	3.529	720	121	
	1.167	0.05	γ	≤ 9.098	0.4	5.1	[38]
	1.169	0.6	α_0	3.620	77.5	82.3	
	1.239	6.1	α_0	3.666	1376	144	
	1.766	3.6	α_0	3.961	4522	800	
^{19}F	0.340 [c]	2.4	$\alpha\gamma$	6.1—7.2	463	102	[22, 95]
	0.872 [c]	4.7	$\alpha\gamma$	6.1—7.2	4095	555	
			$p_3\gamma$	0.197	778	105	
	0.935 [c]	8.1	$\alpha\gamma$	6.1—7.2	2309	182	
			$p_1\gamma$	0.110	1857	146	
	1.088	0.15	$\alpha\gamma$	6.1—7.2	34	144	[22,35,36]
			$p_1\gamma$	0.110	20.1	85	
	[e]		$p_2\gamma$	0.197	347	1473	
^{23}Na	0.592	0.64	$\alpha_0\,(R_\alpha > R_p)$	2.282	311	309	[4, 23, 24]
	1.011	0.5	α_0	2.549	221	281	
			$\alpha_1\gamma$	1.634	30	39	
	1.091	5.0	$\alpha_0\,(R_\alpha < R_p)$	2.601	715	91	
	1.464	1.2	$\alpha_0\,(R_\alpha < R_p)$	2.649	302	160	
			$\alpha_1\gamma$	1.634	77	41	
	1.283	5.5	$\alpha_0\,(R_\alpha < R_p)$	2.726	421	49	
			$p_1\gamma$	0.440	434	50	
	1.457	6.0	$\alpha_0\,(R_\alpha < R_p)$	2.840	122	13	
			$p_1\gamma$	0.440	611	65	
^{24}Mg	0.823	1.3	γ	≥ 3.077	1.2	0.6	
^{27}Al	0.774	0.015	γ	≥ 12.331	4.5	191	[23]
	0.937	0.130	$\alpha_0\,(R_\alpha < R_p)$	1.974	25.5		
	0.992	0.100	γ	≥ 12.542	11.5	73.2	
	1.183	0.660	α_0	2.147	292	282	
	1.364	0.250	α_0	2.275	441	1124	
	1.723	10.0	$\alpha_0\,(R_\alpha < R_p)$	2.529	1299	83	
^{28}Si	3.100	12.5	$p_1\gamma$	1.779	11 565	571	[23]
^{31}P	0.811	0.42	γ	≥ 9.650	3.0	4.5	[23]
	1.018	3.0	$\alpha_0\,(R_\alpha < R_p)$	2.367	101	21.4	
	1.251	1.4	γ	≥ 10.076	9.6	4.4	
	1.438	0.35	γ	≥ 10.257	8.4	15.2	
	1.521	9	$\alpha_0\,(R_\alpha < R_p)$	2.738	2151	152	
^{32}S	3.379	1.0	$p_1\gamma$	2.230	1236	788	[23]

[a] The α-particle energy is given for the angle $\theta = 150°$. For the capture reactions characterized only by γ, the maximal γ-ray energies are given. In the reactions that lead to excited states ($p_1\gamma$) and ($\alpha_1\gamma$), the energy of the transitions with de-excitation is given.
[b] R_α and R_p are the fractions of α particles and protons in the additional absorbers, respectively.
[c] Resonances used to determine hydrogen by interchanging the incident particle and the target nucleus.
[d] "Depth-dependent" by virtue of the broad resonances of the energy of the primary γ rays.
[e] The calculated σ_m exceeds the maximal theoretical value.

well with the depth distributions measured by means of secondary-ion mass spectroscopy.

In this section, we have used a number of special applications to demonstrate the analytic possibilities of the yield functions in the neighborhood of narrow resonances. The main attention has been devoted to nuclei such as fluorine, oxygen, aluminum, and hydrogen in different materials. Of course, more or less narrow resonances also exist in the cross sections of many other reactions due to protons on nuclei that are not considered here. In Table III we have collected together data on the resonances of light nuclei that can be used for similar studies as in the considered examples. Using the resonance parameters given in the reviews of Refs. 18–23, we calculated the corresponding resonance integrals

I_r and the maximal cross sections σ_m at resonance. In accordance with Eq. (15), these quantities characterize the total cross section and can serve as the basis for choosing reactions and resonances suitable for particular analytic tasks. However, it must again be noted that the actually measured yields depend on the differential cross sections, and their angular dependence does not follow from the total cross sections. The procedure for calculating the resonance integrals and the maximal cross sections is given in the Appendix. Thus, for resonances not included in Table III, or for cases for which new experimental results require corresponding corrections, the necessary calculations can be made in a similar way.

4. Broad resonance structures

A broad structure of the cross sections is helpful for determining the total amount of an element and for more extended determination of the depth profiles $N_A(x)$ by means of the radiation spectra measured at fixed energy of the incident particles. If the energy of the bombarding particles is regulated in the region of the plateau of the differential cross section, i.e., $\sigma(\theta, E) \approx \sigma(\theta, E_0)$ in the energy interval ΔE_0, then

i) the integrated radiation yield

$$Y(\theta, E_0) = \frac{\varepsilon n \sigma(\theta, E_0)}{\cos\theta_1} \int_0^{x_0} N_A(x)\, dx \qquad (22)$$

is proportional to the total number of nuclei A in the corresponding region at depth $x \leqslant x_0 = E_0 \cos\theta_1 / [NS_a(E)]$;

ii) in accordance with Eq. (11), the distribution of the spectral intensity $y(\theta, E_0, E)$ gives a representation of the depth distribution $N_A(x)$.

If the half-width of the depth profile is comparable with the depth resolution $\delta t(x)$, the measured energy distribution reflects directly the corresponding depth profile. In other words, the depth profile can be obtained by an unfolding procedure with allowance for the depth-dependent energy resolution $\delta E(x)$. Standard targets with known thickness or area density make it possible to calibrate with respect to the absolute intensity. If the absorption of the γ rays can be ignored, Eq. (22) holds for particles and γ rays. In the case of charged final particles, both the incoming and outgoing particles contribute to the energy-loss factor,[4,14] which is defined as

$$\left|\frac{dE}{dx}\right| = NS_b(E)\left[\frac{1}{\cos\theta_2} + \frac{K_{ab}}{\cos\theta_1}\frac{S_a(E_a)}{S_b(E_b)}\right], \qquad (23)$$

and in accordance with Eqs. (10) and (11) the energy distribution of the emitted charged reaction products is described by

$$y(\theta, E_0, E)\, dE = \frac{\varepsilon n N_A(x)\, \sigma(\theta, E_a(x))\, dE}{NS_b(E)\left[\frac{\cos\theta_1}{\cos\theta_2} + K_{ab}\frac{S_a(E_a)}{S_b(E_b)}\right]}. \qquad (24)$$

Data on the excitation functions or differential cross sections $\sigma(\theta, E)$ are collected together in Refs. 24 and 25 and can be used to select ions with definite energy.

For the spectra of the charged particles, the energy-resolution function $\delta E(x)$ given by Eq. (14) determines depth-dependent contributions $\delta E^a_{st}(x)$ and $\delta E^b_{st}(x)$ of the energy spreading (straggling) of the incident and final particles, respectively,

$$\{\delta E_{st}(x)\}^2 = \{K^2_{ab}(\delta E^a_{st})^2 + (\delta E^b_{st})^2\}, \qquad (25)$$

and the system resolution is characterized by the expression

$$\{\delta F_{sr}\}^2 = \{K^2_{ab}(\delta E_0)^2 + (\delta E_\theta)^2 + (\delta E_{abs})^2 + (\delta E_d)^2\}. \qquad (26)$$

The terms occurring in this expression correspond to the beam energy spread δE_0, the kinematic broadening δE_θ due to the angular spread, the energy spread in the absorbing foil δE_{abs}, and the finite resolution δE_d of the detector. In many cases, the detector itself and the additional absorber limit the energy resolution, and it is only for large depths that the influence of straggling becomes important. On the basis of the energy resolution [see Eq. (14)], the depth resolution can be obtained by means of Eq. (23).

5. Results obtained from particle and γ-ray spectra

For some light nuclei, deuteron-induced reactions enable one to analyze different elements simultaneously. However, because of their rather poor depth resolution ($\delta t > 100$ nm when absorbing foils are used) the (d, p) reactions are usually used to measure element distributions at depths of a few microns, and also to determine the total amounts of elements. As an example, Fig. 17 shows the particle spectrum due to bombardment by 0.66-MeV deuterons of a steel sample subjected to erosion flows of incandescent rocket-fuel gases.[66] The broad proton groups resulting from the $^{12}C(d, p_0)^{13}C$, $^{14}N(d, p_5)^{15}N$, and $^{16}O(d, p_1)^{17}O$ reactions indicate the capacity of the gas components to penetrate into the material of the steel. On the basis of Eq. (6), the maximal yields for the upper energy limits of the proton groups correspond to the concentration at the surface of the sample. The form of the spectral yield of the particles is determined primarily by the product $N_A(x)\sigma(\theta, E_a(x))$, which decreases with the depth. Detailed analysis showed that exposure leads to an increase of the oxygen and nitrogen concentrations down to depths 0.57–0.64 μm, whereas for carbon a concentration in the volume of the sample was determined at depth 0.95 μm. Figure 17 also shows the strong low-energy continuum due to deuteron elastic scattering; this characterizes the counting rate of the detector and is the origin of pulse superposition effects.[67] Here superposition rejection was used to separate the $^{16}O(d, p_1)$ peak from the protruding edge of the deuteron continuum. As was noted earlier, these elastically scattered particles are usually suppressed by calibration absorbing foils. Typical materials for these purposes are mylar ($C_{10}H_8O_4$), aluminum, and gold. Absorbers can also be used to suppress α particles if one is interested in the (d, p) reaction. The stopping powers and ranges of the p, d, and α particles in mylar are tabulated in Ref. 68.

We shall consider in more detail the analysis of oxygen and describe the experimental technique for specific analysis purposes.

In Ref. 69, the thickness and composition of an Al_2O_3 film on an iron alloy were studied by measuring simultaneously the oxygen and aluminum concentrations by means of the $^{16}O(d, p_0)^{17}O$ and $^{27}Al(d, p_{0+1})^{28}Al$ reactions.

In Ref. 70, the diffusion of oxygen, stimulated by heating, in zirconium and a zirconium–copper alloy was investigated by means of the $^{16}O(d, p)^{17}O$ reaction at energy E_d = 823 keV. In the region of this energy, the reaction cross

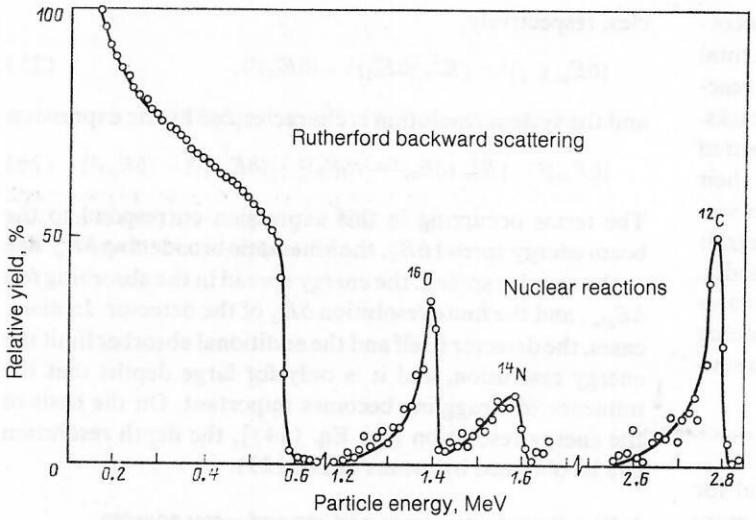

FIG. 17. Groups of protons and elastically scattered incident particles obtained by irradiation with deuterons of a steel sample exposed to high-temperature rocket fuel gases (figure taken from Ref. 66).

section has a plateau, and on the heavy zirconium nuclei competing reactions do not occur. The coefficients of diffusion of oxygen in zirconium were deduced from the oxygen concentration profiles measured to depths of about 180 μm by additional dispersion. Mylar of thickness 13 μm was used to obtain the resolution function, equal to 40 keV for a standard Ta_2O_5 target of thickness 16 nm deposited on tantalum by anodizing.

In Ref. 71, the combined use of the $^{16}O(d, p_1)^{17}O$ nuclear reaction with Rutherford backward scattering and x-ray emission following proton excitation was used for nondestructive analysis of surface oxide films of the bone tip of an arrow with an age of 2200 years. The results show that SnO and CuO are the dominant surface components that prevent corrosion.

Figure 18 demonstrates the simultaneous detection of oxygen atoms on the surface and in deeper layers by means of the $^{16}O(d, p_1)^{17}O$ reaction.[72] A sandwich target (310 nm Co and 330 nm Cr on thick Al) was bombarded by 0.97-MeV deuterons, and the emitted particle spectrum was measured by a surface-barrier detector (diameter 12 mm, $\delta E_d \approx 27$ keV) after passage through a 20-μm mylar foil. For the given geometry ($\Omega = 9$ msr) a beam with deuteron current 30 nA produced 300 counts/sec. There are two clear $^{16}O(d, p_1)$ groups that arise from oxide films on the surface of the cobalt and at the Cr–Al interface. The high-energy tail of the low-energy $^{16}O(d, p_1)$ peak indicates the presence of oxygen impurity even within the chromium layer. The target was inclined at angle $\theta = 45°$, while the detection angle was set at $\theta = 150°$. Thus, the effective range for the particles formed at the Cr–Al interface increased to 1.05 μm. Under the assumption that the surface oxide film was very thin, the width of the energy peak was used to determine the average depth resolution [see Eq. (23)], which was found to be 120 nm on the surface. This is a typical value for (d, p) reactions. To determine oxygen on the surface with high sensitivity, the local maximum of the $^{16}O(d, p_1)^{17}O$ excitation function (see Fig. 5) at $E_d = 0.97$ MeV was chosen. In this case, the cross section was 13×10^{-27} cm^2/sr at 165°.[25] In the deeper layer, the deuteron energy was 0.83 MeV, and the cross section was also reduced, this leading to a decrease of the integrated proton yield. With calibration by means of a thin standard Ta_2O_5 target, the integrated peak intensities correspond to 4.5×10^{16} O/cm^2 (surface) and 8.3×10^{16} O/cm^2 (interface region).

It can be seen from Fig. 5 that at low deuteron energies

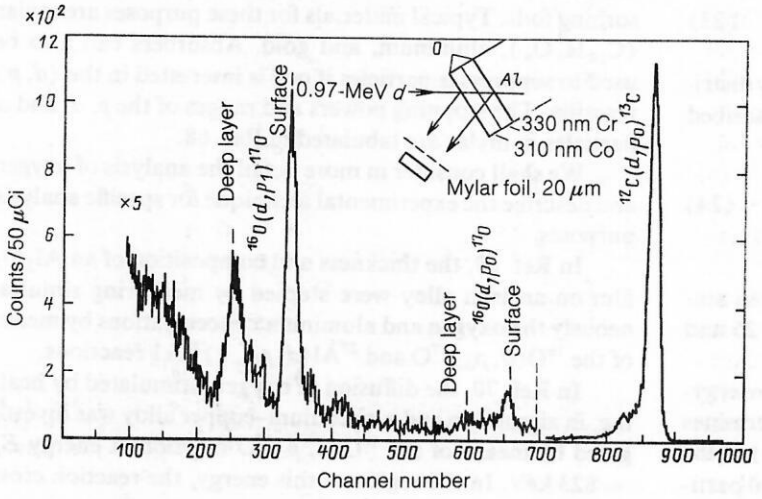

FIG. 18. Proton spectrum measured in the case of deuteron bombardment of a sandwich target with an oxygen-contaminated Cr–Al interface. The detector was shielded by mylar of thickness 20 μm.[72]

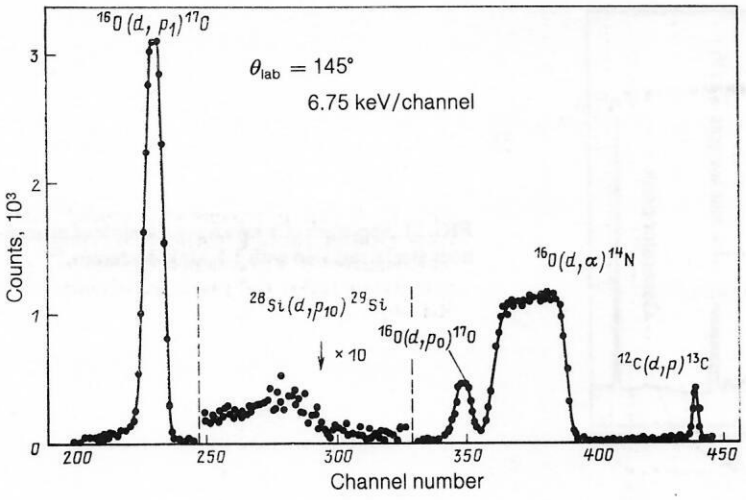

FIG. 19. Particle spectrum from bombardment with 900-keV deuterons of a SiO_2 surface film of thickness 600 nm for normal incidence (figure taken from Ref. 73).

the yield of γ rays from the $^{16}O(d, p\gamma)^{17}O$ reaction is somewhat higher, or, finally, comparable with the $^{16}O(d, p_1)^{17}O$ yield. The total amount of oxygen can be readily measured from the 871-keV peak of the γ rays from the $^{16}O(d, p\gamma)^{17}O$ reaction. In contrast to the analyzed particles, the energy of the γ rays does not depend on the energy of the incident particles, and the angular dependence of the cross section is much weaker.

At the sensitivity limit [usually, this is a quantity of order 10^{13}–10^{14} O/cm^2 in the $^{16}O(d, p_1)^{17}O$ case], the interference with groups of particles from competing reactions has a strong influence. This has already been demonstrated in Fig. 3 in the case of oxygen analysis in a thick silicon sample. The detection limit is here determined by the intensity of the $^{28}Si(d, p_{10})$ group, which interferes with the $^{16}O(d, p_1)$ proton peak.

For final particles with large stopping cross section S_b the energy-loss factor is increased [see Eq. (23)]. Thus, the depth resolution for the $^{16}O(d, \alpha)^{14}N$ reaction is better than the resolution for the $^{16}O(d, p_0)^{17}O$ reaction, as is shown in Fig. 19, which gives the particle spectrum obtained from deuteron bombardment from a SiO_2 surface film of thickness 0.6 μm on silicon.[73] At deuteron energies $E_d \lesssim 1$ MeV and $\theta = 165°$ the cross sections of the two reactions are about the same.[25] To maintain the resolution at the level 20–40 nm at depth 0.2–1.5 μm there is no need to place any foils in front of the detector. Therefore, one can use beams with a low current if one simultaneously increases the irradiation time, usually to a few hours per spectrum.[74] A further improvement of the depth resolution can be achieved by inclining the target. In Ref. 74, the oxygen distribution in an aluminum film of thickness 220 nm deposited on a layer of solid silver was analyzed. The results are shown in Fig. 20. In the aluminum film, the atomic concentration of the oxygen was 6%. Grazing incidence improved the surface depth resolution by four times.

Usually, the α-particle spectrum from the $^{16}O(d, \alpha_0)^{14}N$ reaction interferes with the high-energy proton groups from the $^{16}O(d, p_0)$ and $^{12}C(d, p_0)$ reactions. It was shown in Ref. 74 that this effect can be prevented if the inclination of the detector is reduced. Similar advantages of thin depleted regions are obtained when low-energy particles are extracted in the presence of strong β radiation induced by radioactivity of the target.[5] To maintain a good resolution, the use of detectors with a low resistivity is recommended.[74]

In experiments with very good resolution,[75] with analysis of the final particles by means of a magnetic spectrometer, Ta_2O_5 170-nm films on silicon were bombarded with 0.9-MeV deuterons with normal incidence. A depth resolution of 17 nm for the $^{16}O(d, \alpha_0)$ distribution and 50 nm for the $^{16}O(d, p_1)$ group was obtained. In such a case, there is no need to use absorbing foils but the simultaneous determination of different isotopes is no longer possible.

Similarly, for oxygen detection the (d, α), (d, p), and $(d, p\gamma)$ reactions can also be used to measure the ^{14}N concentration and its depth profile. The $^{14}N(d, \alpha)^{12}C$ reaction makes it possible to determine depth profiles with good resolution. However, the cross sections are in this case four times smaller than the cross section of the $^{16}O(d, \alpha)^{14}N$ reaction.

In Ref. 77, a beam of 1.55-MeV deuterons with a 1-mm beam spot was used for the surface scanning of samples of industrial glasses. Analysis of the yield of the $^{14}N(d, \alpha_0)$ particles as a function of the beam position revealed strong nonuniformity in the surface distribution of the nitrogen. At beam current 10 nA, about two hours were needed to scan a

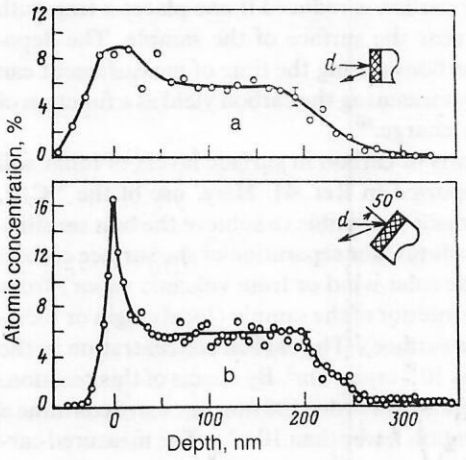

FIG. 20. Hydrogen-concentration profile obtained by means of a $^{16}O(d, \alpha)$ energy analysis of a 220-nm aluminum film for normal (a) and grazing (b) angles of incidence of a beam of 900-keV deuterons (figure taken from Ref. 74).

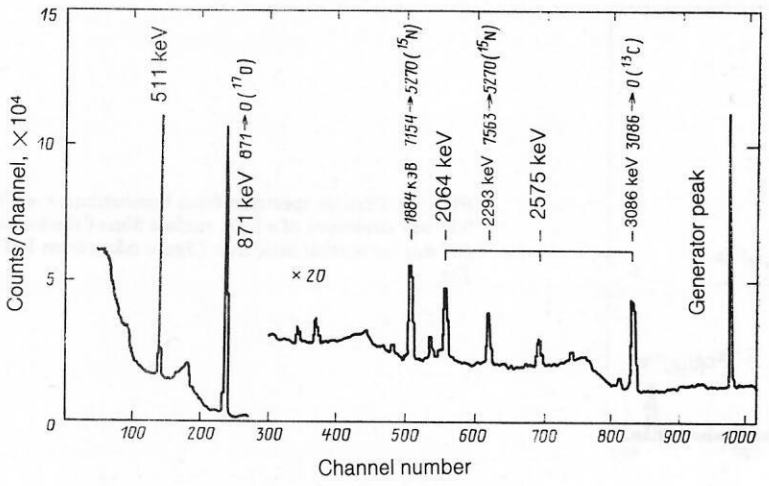

FIG. 21. Spectrum of γ rays from a sample of nitrogenous steel irradiated with 1.5-MeV deuterons.[72]

sample containing 10^{-5} g of dissolved nitrogen. To study the ^{14}N profiles in nitrogenous steels to a depth of about 30 μm, Harwell microprobes were used in Refs. 78 and 79. The vertical structures were lengthened to several hundred microns by oblique sections and scanning by means of a deuteron microbeam with a 10×30 μm spot; the integrated intensities of the $^{14}N(d, p_0)$ and $N(d, \alpha_0)$ particle groups were determined. The yields were converted into element concentrations by means of Si_3N_4 standards. For example, the investigations of Ref. 79 show that preferential deposition of titanium nitride prevents the penetration of nitrogen into the thickness of the sample.

In Ref. 79, the same experimental method was used to investigate the diffusion of carbon in fast-reactor steels by using the very effective $^{12}C(d, p_0)^{13}C$ reaction at energy $E_d = 1.3$ MeV. Compared with the $^{16}O(d, p_1)^{17}O$ reaction, the cross section of this reaction is an order of magnitude higher. In the study of carbon and nitrogen by means of microbeams, sensitivity limits for the concentration of order 10^{-4} g were established.[78] The determination of low carbon concentrations is influenced by deposition and irradiation damage of hydrocarbons. Similar systematic experiments were made in Ref. 80, and these also revealed that an ion beam stimulated the growth or decay of oxygen on the surface of silicon and copper targets, respectively. The contamination of the surface by carbon is reduced if one places a trap with liquid nitrogen near the surface of the sample. The deposition of hydrocarbons during the time of measurement can be determined by measuring the carbon yield as a function of the adsorbed ion charge.[80]

Measurements of carbon in surface layers of lunar soil samples were reported in Ref. 41. Here, use of the $^{12}C(d, p_0)^{13}C$ reaction made it possible to achieve the best sensitivity and depth resolution for separation of the surface carbon (implanted by the solar wind or from volcanic vapor) from the carbon in the interior of the sample (local origin or redistributed from the surface). The carbon concentration in the surface layers was 10^{13} atom/cm^2. By means of this reaction, with a depth resolution of order 100 nm, one can determine a volume concentration lower than 10^{-4} g. The measured carbon spectra indicate interference with other reactions induced by deuterons under the influence of ^{27}Al, ^{28}Si, and ^{24}Mg. The peaks in the measured spectra were identified by means of appropriate standard samples.

In the following example, we consider the absorption of carbon monoxide on a platinum surface.[82] At deuteron energy 0.97 MeV, both the $^{12}C(d, p_0)^{13}C$ and the $^{16}O(d, p_1)^{17}O$ reaction were used for simultaneous determination of carbon and oxygen. Therefore, the C–O stoichiometry could be readily verified. The $^{12}C(d, p)^{13}C$ reaction was calibrated relative to the $^{16}O(d, p_1)^{17}O$ reaction by frozen CO_2 as a secondary standard. To prevent erosion of the frozen gas films, the dose of the bombarding $^2H^+$ was limited to 2 μCi in a beam spot of 3 mm^2.

When carbon is bombarded with deuterons, ^{13}C excited states are also populated, as shown by the emission of strong γ rays. As an example, Fig. 21 shows the γ-ray spectrum from a steel sample bombarded by 1.5-MeV deuterons. The γ-ray spectrum was observed by means of a Ge(Li) detector of volume 80 cm^3 (resolution 5.7 keV for the 2.6-MeV line) at a distance of 4 cm from the target. One can clearly see the γ-ray peaks of the $^{12}C(d, p_0)^{13}C$ reaction with energy 3086 keV and the corresponding leakage peaks, indicated by the brackets. One can also see peaks corresponding to the reactions $^{16}O(d, p_0)^{17}O$ (871 keV) and $^{14}N(d, p\gamma)^{15}N$ (2293 and 1884 keV). The origin of these two nitrogen peaks is associated with different transitions in ^{15}N, as follows from Fig. 21. The integrated intensities of the peaks were used to determine the total amounts of C, O, and N.

In Fig. 22, we compare the yield functions of the $^{12}C(d,$

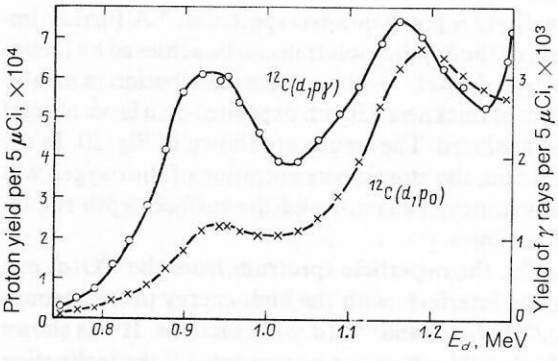

FIG. 22. Yield curves for $^{12}C(d, p_0)$ and $^{12}C(d, p\gamma)$ reactions. The γ-ray yield from the 80-nm carbon target on tantalum was measured by means of a Ge(Li) detector of volume 40 cm^3 at distance 40 mm from the target. The solid angle of the particle detector was 9 msr.[72]

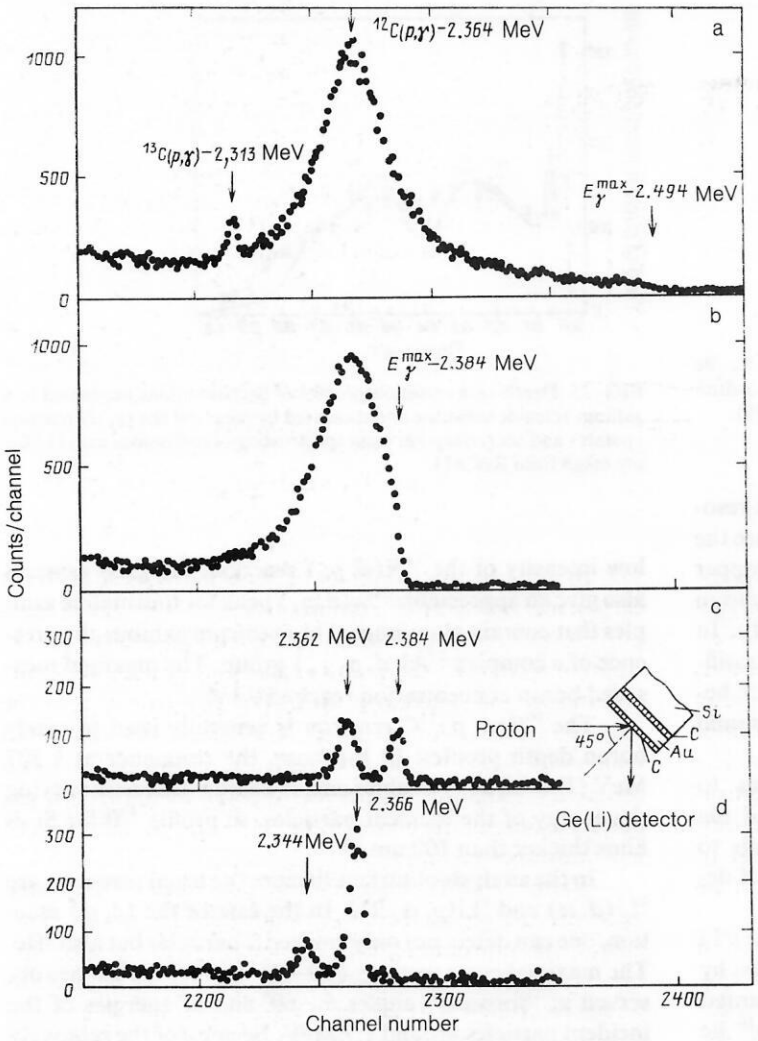

FIG. 23. Spectra of γ rays from the $^{12}C(p, \gamma)^{13}N$ reaction measured in the region of the resonance with energy $E_p = 0.457$ MeV The spectra from the thick targets at 0.596 MeV (a) and 0.477 MeV (b) show that there exists a resonance of the first excited state of ^{13}N and a cutoff at E_γ^{max} equal to 2.494 MeV and 2.384 MeV, respectively. Well defined γ-ray peaks are observed for sandwich targets at energies $E_p = 0.477$ MeV (c) and 0.457 MeV (d) (figure taken from Ref. 83).

p_0) and $^{12}C(d, p\gamma)$ reactions for the region of incident-particle energies $E_d = 0.7$–1.3 MeV.[72] The two yield curves were measured simultaneously by means of a Ge(Li) detector of volume 40 cm^3 and a surface-barrier detector of diameter 12 mm at detection angles 90 and 150°, respectively. Basically, the (d, p_0) contribution is dominant (greater by about an order of magnitude), and the particle channel is assumed to be the most suitable for carbon determination.

Usually, γ-ray spectra measured at fixed energies of the incident particles do not give any information about the depth profiling. An exception to this rule is provided by primary γ rays emitted in capture reactions (considered in Sec. 2.2; see Fig. 7). The energies of these primary γ rays depend on the actual energy of the captured incident particle. Therefore, for given incident energy E_0 the emitted energy of the γ rays depends on the depth.

In Ref. 76, the $^{16}O(p, \gamma)^{17}F$ reaction was used to investigate oxide films, and it was shown that direct capture of protons leads to depth-dependent γ-ray energies. The direct capture process is manifested in the smoothed behavior of the cross section of these reactions at proton energies $E_p \leqslant 1.5$ MeV. In contrast, the cross section of the $^{12}C(p, \gamma)^{13}N$ reaction has a broad resonance ($\Gamma = 36$ keV) near $E_c = 0.457$ MeV, this corresponding to the first excited ^{13}N state. In Ref. 83 the present authors and collaborators reported carbon depth profiling by means of γ-ray spectroscopy at fixed energy of the incident protons. The results are given in Fig. 23. These are spectra measured for a target of reactor graphite and for sandwich structures (10 nm C + 100 nm Au + 10 nm C) on a thick silicon sample. The upper curves were obtained by bombardment of a thick graphite target with protons of energy 0.596 and 0.477 MeV, respectively. It can be seen that the maximum of the γ-ray energy depends on the energy of the incident protons, and for higher proton energies the broad γ-ray peak reflects the shape of the resonance. On the basis of Eq. (1), the maximal γ-ray energy is described by the formula

$$E_\gamma^{max} = Q_0 + \frac{m(^{12}C)}{m(^{12}C) + m(^1H)} E_p, \qquad (27)$$

in accordance with the direct capture process. For the $^{12}C(p, \gamma)$ reaction, the Q value is given as $Q_0 = 1.943$ MeV. In the lower part of Fig. 23 we show the well-resolved γ-ray peaks from carbon on the surface and from a deeper layer. The intensities of the peaks depend on the energy of the incident particles in accordance with the form of the cross section. Unfortunately, the cross sections of both of the reactions $^{16}O(p, \gamma)$ and $^{12}C(p, \gamma)$ are very small, and their use is very limited.

The $^9Be(p, d)^8Be$ and $^9Be(p, \alpha)^6Li$ yield functions have broad resonances in the region of 0.35 MeV with cross sections $(20$–$30) \times 10^{-27}$ cm^2/sr at detection angle $\theta = 138°$.

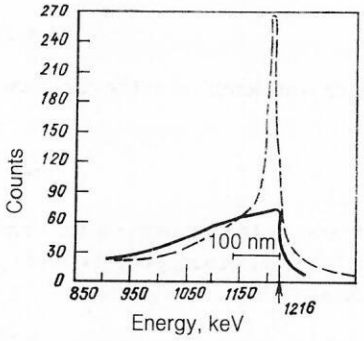

FIG. 24. Energy distribution of groups of α particles emitted by a Cu–Be alloy irradiated with 300-keV protons after annealing at 525 °C (continuous curve) and 885 °C (broken curve) (figure taken from Ref. 84).

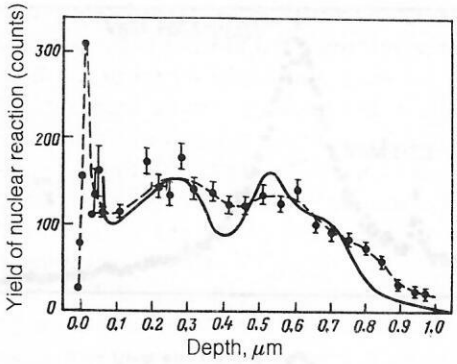

FIG. 25. Depth concentration profiles of beryllium ions implanted in a gallium arsenide substrate and measured by means of the (p, α) reaction (points) and secondary-ion mass spectroscopy (continuous curve) (figure taken from Ref. 87).

The (p, α) reaction is well suited to analysis with high resolution near a surface and was used in Ref. 84 to measure the induced activity of beryllium implanted in nickel and copper samples. As is shown in Fig. 24, a constant Be concentration gives a weakly decreasing yield with increasing depth. In contrast to this, one observes a pronounced surface stratification due to the annealing process, as a result of which beryllium oxidation on the surface is favored. The nominal depth resolution was 15 nm.

To measure the total beryllium concentrations to depths of a few microns, both the $^9\mathrm{Be}(p, d_0)^9\mathrm{Be}$ and the $^9\mathrm{Be}(p, \alpha\gamma)^6\mathrm{Li}$ reaction are preferred. The latter leads to emission of γ rays with energy 2.19 MeV as a result of deexcitation of the first excited state of the ^{6}Li nucleus.

In Ref. 85, the results of analysis using the $^9\mathrm{Be}(p, \alpha)^6\mathrm{Li}$ reaction were compared with the results of measurement by mass spectroscopy of secondary ions of layerwise implanted beryllium in the first micron of a GaAs matrix (10^{16} Be atom/cm^2, 110 keV). It can be seen from Fig. 25 that after annealing for 30 min at 800 °C the (p, α) reaction reveals a strong surface stratification of beryllium, which could not be observed by secondary-ion mass spectroscopy. The chosen beam energy was $E_p = 2.25$ MeV, which is at the maximum of the cross section (14×10^{27} cm^2/sr at 45°).[85] A proton beam with energy spread $\delta E_0 \approx 1$ keV was used; the energy resolution of the double focusing magnetic spectrometer with position-sensitive detector was 3.2 keV. A depth resolution of about 10 nm was obtained from the width of the beryllium surface peak. At depth 200 nm, the energy spread became the main reason for the deterioration in the depth resolution.

Beryllium can also be analyzed by means of incident deuterons by using the $^9\mathrm{Be}(d, p_0)^{10}\mathrm{Be}$ or $^9\mathrm{Be}(d, \alpha)^7\mathrm{Li}$ reactions. This may be of interest for the simultaneous determination of beryllium with other light elements.[68]

For measurement of the total number of boron atoms it is advisable to use the $^{10}\mathrm{B}(d, p)^{11}\mathrm{B}$ reaction. In thermally deposited films of boron on silicon plates, not only the Si–B phase but also the B_6O component was found by simultaneous detection of ^{10}B and ^{16}O.[87] The detector was covered by a mylar film of thickness 32 μm to suppress interference of the (d, α) reaction.

The (d, p) reaction was also used in Ref. 87 to study boron in tourmaline in boron–silicate glasses.

It was shown that the $^{10}\mathrm{B}(d, \mathrm{p}_0)$ yield at $E_d \approx 2$–3 MeV is approximately constant at detection angle 30°. Besides the low intensity of the $^{14}\mathrm{N}(d, p_0)$ reaction, the glass samples also give an appreciable $^{28}\mathrm{Si}(d, p_1)$ peak for tourmaline samples that contain aluminum. The spectrum exhibits the presence of a complex $^{27}\mathrm{Al}(d, p_{0+1})$ group. The maximal measured boron concentration reached 0.1%.

The $^{10}\mathrm{B}(\alpha, p)^{13}\mathrm{C}$ reaction is generally used to syudy boron depth profiles. In this case, the resonance at 1.507 MeV ($\Gamma = 18$ keV) enables one, in conjunction with varying the energy of the incident particles, to profile ^{10}B for Si–B films thicker than 100 nm.[88]

In the analysis of surface lithium the usual reactions are $^6\mathrm{Li}(d, \alpha)$ and $^6\mathrm{Li}(p, \alpha)^3\mathrm{He}$. In the case of the (p, α) reaction, one can detect not only emitted α particles but also ^{3}He. The maximal cross sections $(10\text{–}40)\times10^{-27}$ cm^2/sr are observed at "forward" angles $\theta < 60°$ and at energies of the incident particles around 1.7 MeV. Because of the relatively small Q ($Q_0 \approx 4$ MeV), it is not advisable to use the (p, α) channel in connection with an additional absorber. Therefore, preference is usually given to the (d, α) reaction, which is characterized by a smoothed form of the cross section with a maximum 6×10^{-27} cm^2/sr for deuteron energy around 0.6 MeV.

The (d, α) reaction was used in Ref. 89 to determine the diffusion coefficient from depth-profile measurements. A strongly reduced diffusion coefficient was found, this being the result of radiation damage during implantation of the ions. A clear surface peak revealing capture of the diffusing lithium at the surface was also found.

Finally, we discuss some aspects of deuterium analysis. In practice, deuterium is detected by means of two reactions: $^2\mathrm{H}(d, p)^3\mathrm{H}$ or $^2\mathrm{H}(^3\mathrm{He}, p)^4\mathrm{He}$. The second is often recommended because of the large Q ($Q_0 \approx 18$ MeV) and large cross section. However, most accelerators give deuterons and not ^{3}He ions. Therefore, in practice the use of the $^2\mathrm{H}(d, p)^3\mathrm{H}$ reaction is more typical. For an energy of this reaction above 1 MeV the cross section is approximately constant (about 8×10^{-27} cm^2/sr).

The diffusion of implanted deuterium ions in nickel was contrasted with the accumulation of deuterium from the gas phase on a platinum surface.[89] Depth profiles were observed by means of the $^2\mathrm{H}(d, p)^3\mathrm{H}$ reaction at $E_d = 2$ MeV. Only when the surface of the sample was contaminated from the gas phase were diffusion coefficients typical for undamaged materials obtained. The profiles of deuterium ions implant-

ed in solid nickel targets were used in Ref. 90 to obtain a good depth resolution, the absorbing foil in front of the detector being replaced by an electrostatic-field separator. At high implantation fluxes of the deuterons (more than 3×10^{18} $^2H/cm^2$) appreciable secondary emission was obtained; it was explained by the effects of blistering.[91] Capture by defects of implanted deuterium ions in aluminum was studied in Ref. 92. Whereas the deuterium depth profiles were measured by means of the $^2H(^3He, p)^4He$ reaction after annealing at different temperatures, the total amount of deuterium was observed by means of the $^2H(d, p)^3H$ reaction at energy $E_d = 0.8$ MeV. The detector was shielded by a 12-μm mylar foil containing several small openings, and the depth of the active zone of the detector was 300 μm.

Nuclear reactions are specific for each isotope [see Eq. (5)] and, therefore, are an excellent basis for methods of determining traces of elements. The possibilities of reactions induced by deuterons and protons for detecting ^{13}C and ^{15}N in connection with the Harwell microprobes were demonstrated in Ref. 96.

The examples that have been discussed in the present section have been limited to the most widely used reactions. A fuller list of the reactions and also the reconmended energies of the incident particles and the experimental parameters are published in Ref. 24.

4. CONCLUSIONS

The use of nuclear resonance reactions for surface analysis of solids has been demonstrated for a large number of examples—from the technology of the production of semiconductor electronic devices to the investigation of geological and archeological samples. We have considered yield curves in the neighborhood of narrow resonances, and also the measured emission spectra at fixed energies of the incident ions. In summary, we can say that in many cases nuclear resonance reactions represent a valuable extension of the analytic methods of investigation.

Modern tendencies in this field are associated with the use of different analytic methods that complement each other, while at the same time the analytic possibilities such as the sensitivity, lateral resolution, and depth resolution are improved. In this direction, the development of ion microbeams opens up new possibilities. The surface distribution and the depth distribution of individual isotopes or nuclei can, finally, be measured simultaneously if charged final particles are used for identification.

APPENDIX: CALCULATION OF MAXIMAL RESONANCE CROSS SECTIONS AND RESONANCE INTEGRALS

In the literature, resonances are frequently characterized by the resonance energy E and the total width Γ determined in the laboratory system, and also by the normalized yields Y_N of the resonances[18-23]

$$Y_N = (2J+1)\frac{\Gamma_a\Gamma_b}{\Gamma}\,. \tag{A.1}$$

Here, J is the total spin of the state of the compound nucleus that gives the corresponding resonance. The partial widths Γ_a and Γ_b characterize the entrance and exit channels of the $A(a,b)B$ reactions, and the total width Γ is the sum of all the partial widths. The maximal cross section contained in the Breit–Wigner formula [see Eq. (16)] is given as

$$\sigma_m = \pi\lambda\!\!\!^{-2} g\,\frac{\Gamma_a\Gamma_b}{(\Gamma/2)^2}\,, \tag{A.2}$$

where the reduced de Broglie wavelength $\lambda\!\!\!^{-}$ in the center-of-mass system is

$$\lambda\!\!\!^{-} = \frac{\hbar}{(2\mu E')^{1/2}}\,, \tag{A.3}$$

in which μ is the reduced mass of the incident particle and the target nucleus and E' is the kinetic energy of the colliding partners in the center-of-mass system. This gives

$$\pi\lambda\!\!\!^{-2} = 0{,}652\cdot10^{-24}\left(\frac{m_a+m_A}{m_A}\right)^2\frac{1}{A_aE}\,, \tag{A.4}$$

where A_a is the mass number of the incident particle a, and E is the energy of the incident particle in the laboratory system. The statistical factor

$$g = \frac{2J+1}{(2s+1)(2J_0+1)} \tag{A.5}$$

depends on the known spins s and J_0 of the incident particle and the target nucleus in their ground states, respectively, and often on the unknown spin J of the compound nucleus.

The ratio Γ_b/Γ describes the probability that the compound state will decay into the final channel b. This channel describes the transition to a definite state of the resulting nucleus.

For narrow resonances, the condition $\Gamma \ll E$ is almost always satisfied, and the resonance integral is

$$I_r = \int_{-\infty}^{\infty}\sigma(E)\,dE = \frac{\pi}{2}\Gamma\sigma_m \tag{A.6}$$

or

$$I_r = \frac{2(\pi\lambda\!\!\!^{-})^2}{(2s+1)(2J_0+1)}(2J+1)\frac{\Gamma_a\Gamma_b}{\Gamma}\,. \tag{A.7}$$

For the calculation of this integral, the de Broglie wavelength is assumed to be constant in the region of the narrow resonance. The ground-state spins s and J_0 are known from the literature,[18-23] and $(\pi\lambda\!\!\!^{-})^2$ is determined from Eq. (A.4). Therefore, using the normalized yields, one can calculate the resonance integral, and from Eq. (A.6) one can obtain the value of the maximal cross section

$$\sigma_m = \frac{2I_r}{\pi\Gamma}\,. \tag{A.8}$$

In accordance with Eq. (10) for a thin surface target the maximal resonance yield is given as

$$dY_m(E = E_r) = \varepsilon n\sigma_m N_A\,dx/\cos\theta_1,$$

whereas for a thick target with $N_A(x) = \text{const}$ the height of the step function due to the resonance is described as

$$\Delta_r = \varepsilon n N_A\int\frac{\sigma(E)\,dE}{N_M S_M(E)} = \varepsilon n\frac{N_A}{N_M S_M(E_r)}I_r\,. \tag{A.9}$$

Here, the total atomic density N_M and the mean stopping cross section $S_M(E_r)$, taken for the resonance energy E_r, characterize the energy loss in the multicomponent material in accordance with Eq. (8). If the γ-ray absorption is ignored, Eq. (A.9) is valid for particles and γ rays.

[1]J. F. Ziegler (ed.), New Uses of Ion Accelerators, Plenum Press, New York (1975).
[2]T. A. Cahill, "Ion-excited x-ray analysis of environmental samples," in Ref. 1, p. 1.

[3]J. A. Cairns and L. C. Feldman, "Ion-induced x-rays in solids," in Ref. 1, p. 431.
[4]W. K. Chu, J. W. Mayer, and M. A. Nicolet, Backscattering Spectrometry, Academic Press, New York (1978).
[5]G. Amsel, J. P. Nadai, E. D'Artemare, *et al.*, "Microanalysis by the direct observation of nuclear reactions using a 2 MeV van de Graaff," Nucl. Instrum. Methods **92**, 481 (1971); see also Ref. 93.
[6]E. A. Wolicki, "Material analysis by means of nuclear reactions," in Ref. 1, p. 159.
H. E. Grove and A. E. Litherland, "Gamma-rays from unbound nuclear states formed by charged-particle capture," in: Nuclear Spectroscopy (ed. F. Ajzenberg-Selove), Academic Press, New York (1960), Part A, p. 260.
[8]A. H. F. Muggleton, "Semiconductor devices for gamma-ray, x-ray and nuclear radiation detection," J. Phys. E **5**, 390 (1972).
[9]J M. McKenzie "Development of the semiconductor radiation detector," Sandia Laboratory Report SAND 78-1114, December (1978).
[10]R. A. Langley, "Instrumentation and experimental techniques," in Ref. 4, p. 153.
[11]F. Watt, G. W. Grime, G. W. Blower, *et al.*, "The Oxford 1 μm proton microprobe," Nucl. Instrum. Methods **197**, 65 (1982).
[12]H. Kneis, B. Martin, R. Nobiling, *et al.*, "The Heidelberg proton microprobe," Nucl. Instrum. Methods **197**, 79 (1982).
[13]G. Deconninck and F. Bodart, "New developments in nonvacuum analysis," Nucl. Instrum. Methods **149**, 609 (1978).
[14]G. Deconninck, Introduction to Radioanalytical Physics, Akademiai Kiado, Budapest (1978).
[15]J. F. Ziegler, Handbook of Stopping Cross Sections for Energetic Ions in All Elements, Pergamon Press, New York (1980).
[16]S. Fiarman and S. S. Hanna, "Energy levels of light nuclei $A = 3$," Nucl. Phys. **A251**, 1 (1975).
[17]S. Fiarman and W. E. Meyerhof, "Energy levels of light nuclei $A = 4$," Nucl. Phys. **A206**, 1 (1973).
[18]F. Ajzenberg-Selov, "Energy levels of light nuclei $A = 5$–10," Nucl. Phys. **A320**, 1 (1979).
[19]F. Ajzenberg-Selove and C. L. Busch, "Energy levels of light nuclei $A = 11$–12," Nucl. Phys. **A336**, 1 (1980).
[20]F. Ajzenberg-Selove, "Energy levels of light nuclei $A = 13$–15," Nucl. Phys. **A360**, 1 (1981).
[21]F. Ajzenberg-Selove, "Energy levels of light nuclei $A = 16$–17," Nucl. Phys. **A375**, 1 (1982).
[22]F. Ajzenberg-Selove, "Energy levels of light nuclei $A = 18$–20," Nucl. Phys. **A392**, 1 (1983).
[23]P. M. Endt and C. van der Leun, "Energy levels of $A = 21$–44 nuclei (VI)," Nucl. Phys. **A310**, 1 (1978).
[24]J. W. Mayer and E. Rimini (eds.), Ion Beam Handbook for Material Analysis, Academic Press, New York (1977).
[25]R. A. Jarjis, Nuclear Cross Section Data for Surface Analysis, Department of Physics Schuster Laboratory, The University, Manchester, N13 9PL, England, December (1979).
[26]J. R. Bird, "Nuclear cross-sections for ion beam analysis," Nucl. Instrum. Methods **168**, 85 (1980).
[27]G. Deconninck, G. Demortier, and F. Bodart (eds.), Chemical Analysis by Charged Particle Bombardment (Proc. of the International Meeting, Namur, Belgium 6–8 September, 1971), Elsevier Sequoia S. A., Lausanne (1972).
[28]J. W. Mayer and J. F. Ziegler (eds.), Ion Beam Surface Layer Analysis, Elsevier Sequoia S. A., Lausanne (1974).
[29]O. Meyer, G. Linker, and F. Käppeler (eds.), Ion Beam Surface Layer Analysis (Proc. of the International Conference on Ion Beam Surface Layer Analysis, Karlsruhe, 15–19 September, 1975), Plenum Press, New York (1975).
[30]J. W. Butler, C. M. Davisson, and P. A. Treado, Proc. of the Third International Conference on Ion Beam Analysis, Washington, D. C., 1977, in: Nucl. Instrum. Methods **149**, 193 (1978).
[31]H. H. Andersen, J. Böttiger, and H. Knudsen (eds.), Proc. of the Fourth International Conference on Ion Beam Analysis, in: Nucl. Instrum. Methods **168**, (1980).
[32]J. R. Bird *et al.*, Proc. of the Fifth International Conference on Ion Beam Analysis, Sydney 1981, in: Nucl. Instrum. Methods **191** (1981).
[32]G. Demortier (ed.), Microanalysis Using Charged Particle Accelerators. Proc. of the Second International Conference on Chemical Analysis, Namur, Belgium, 8–10 September, 1981, in: Nucl. Instrum. Methods **197** (1982).
[34]J. Stroobants, F. Bodart, G. Deconninck, *et al.*, "Analysis of fluorine by nuclear reactions and application to human dental enamel," in Ref. 29, Vol. 2, p. 933.
[35]D. Dieumegard, B. Maurel, and G. Amsel, "Microanalysis of fluorine by nuclear reactions. I. $^{19}F(p, \alpha_0)^{16}O$ and $^{19}F(p\alpha\gamma)^{16}O$ reactions," Nucl. Instrum. Methods **168**, 93 (1980).
D. Grambole *et al.*, "Fluorine detection in the near surface region of solids using the $^{19}F(p,p'\gamma)^{19}F$ reaction," to be published in J. Radioanal. Chem.
[37]E. Möller and N. Starfelt, "Microanalysis of fluorine in zircaloy by the use of the $^{19}F(p, \alpha\gamma)^{16}O$ reaction," Nucl. Instrum. Methods **50**, 225 (1967).
[38]B. Maurel, G. Amsel, and J. P. Nadai, "Depth profiling with narrow resonances of nuclear reactions: theory and experimental use," Nucl. Instrum. Methods **197**, 1 (1982).
[39]F. Bodart and G. Deconninck "Concentration depth profiling in fluorine implanted iron," Nucl. Instrum. Methods **197**, 59 (1982).
[40]J. W. Handler, R. B. Moler, E. Raisen, and K. S. Rajan, Thin Solid Films **19**, 165 (1973).
[41]T. A. Tombrello, "Ion-beam analysis of meteoritic and lunar samples," Nucl. Instrum. Methods **168**, 459 (1980).
[42]G. E. Coote, R. J. Sparks, and P. Blattner, "Nuclear microprobe measurement of fluorine concentration profiles, with application in archaeology and geology," Nucl. Instrum. Methods **197**, 213 (1982).
[43]P. Gippner, C. Bauer, K. Hohmuth, *et al.*, "Detection of fluorine contamination by means of the $^{19}F(p, p'\gamma)^{19}F$ reaction," Nucl. Instrum. Methods **191**, 341 (1981).
[44]R. E. Shroy, H. W. Kraner, K. W. Jones, *et al.*, "Determination of fluorine in food samples by the $^{19}F(p,p'\gamma)^{19}F$ reaction," Nucl. Instrum. Methods **149**, 313 (1978).
[45]A. Z. Hrynkiewicz, S. Szymczyk, J. Kajfosz, and M. Olech, "PIXE and NRA environmental studies by means of lichen indicators," Nucl. Instrum. Methods **168**, 517 (1980).
[46]G. E. Coote, N. E. Whitehead, and G. J. McCallum, "A rapid method of obsidian characterization by inelastic scattering of protons," J. Radioanal. Chem. **12**, 491 (1972).
[47]M. J. Kenny, J. R. Bird, and E. Clayton, "Proton induced γ-ray yields," Nucl. Instrum. Methods **168**, 115 (1980).
[48]G. Deconninck and G. Demortier, "Quantitative analysis of aluminum by prompt nuclear reactions," J. Radioanal. Chem. **12**, 189 (1972).
[49]M. A. Meyer, I. Venter, and D. Reitmann, "Energy levels of ^{28}Si," Nucl. Phys. **A250**, 235 (1975).
[50]M. K. Bernett, J. W. Butler, E. A. Wolicky, and W. A. Zisman, "Relation between residual polishing agent and material hardness determined by a narrow nuclear-reaction resonance technique," J. Appl. Phys. **42**, 5826 (1971).
[51]J. R. Cameron, "Elastic scattering of alpha-particles by oxygen," Phys. Rev. **90**, 839 (1953).
[52]G. Mezey, J. Gyulai, T. Nagy, *et al.*, "Enhanced sensitivity of oxygen detection by the 3.05 MeV (α, α) elastic scattering," in Ref. 29, p. 293.
[53]S. Petersson, H. Norde, G. Possnert, and B. Orre, "Oxygen distribution profiles in thin evaporated contacts on single crystal silicon," Nucl. Instrum. Methods **149**, 285 (1978).
[54]J. P. Ponpon, J. J. Grob, A. Grob, *et al.*, "Interface studies of metal–semiconductor contacts by means of SINS, nuclear reactions and RBS," Nucl. Instrum. Methods **149**, 647 (1978).
[55]C. D. Mackenzie and B. H. Armitage, "Pore size from resonance charged particle backscattering," in Ref. 29, p. 281.
[56]K. L. Dunning, "$^{27}Al(p, \alpha_0)^{24}Mg$ resonance profiling of aluminum in silicon-on-sapphire materials," Nucl. Instrum. Methods **149**, 317 (1978).
[57]R. L. Kauffman, L. C. Feldman, and R. P. H. Chang, "Use of ion beam techniques to characterize thin plasma grown GaAs and Ga AlAs oxide films," Nucl. Instrum. Methods **149**, 619 (1978).
[58]D. A. Leich and T. A. Tombrello, "A technique for measuring hydrogen concentration versus depth in solid samples," Nucl. Instrum. Methods **108**, 67 (1973).
[59]J. F. Ziegler, C. P. Wu, P. Williams, *et al.*, "Profiling hydrogen in materials using ion beams," Nucl. Instrum. Methods **149**, 19 (1978).
[60]G. J. Clark, C. W. White, D. D. Allred, *et al.*, "The application of nuclear reactions for quantitative hydrogen analysis in a variety of different materials problems," Nucl. Instrum. Methods **149**, 9 (1978).
[61]W. A. Lanford, "^{15}N hydrogen profiling: scientific applications," Nucl. Instrum. Methods **149**, 1 (1978).
[62]J. P. Bugeat and E. Ligeon, "Influence of ion beam bombardment in hydrogen surface layer analysis," Nucl. Instrum. Methods **159**, 117 (1979).
[63]E. Ligeon, A. Guivarc'h, J. Fontenille, *et al.*, "Nuclear reaction analysis of hydrogen in amorphous silicon and carbide films," Nucl. Instrum. Methods **168**, 499 (1980).
[64]P. Trocellier, B. Nens, and Ch. Engelman, "Measurements of the hydrogen, sodium and aluminum concentration versus depth in the near surface region of glasses by resonant nuclear reactions," Nucl. Instrum. Methods **197**, 15 (1982).
[65]I. S. T. Tsong, H. D. Monkowski, J. R. Monkowski, *et al.*, "Hydrogen and chlorine detection at the SiO_2/Si interface," Nucl. Instrum. Meth-

ods **191**, 91 (1981).
[66]A. Niiler and R. Birkmire "Measurement of oxygen and nitrogen profiles in steel," Nucl. Instrum. Methods **149**, 301 (1978); "The $^{14}N(d, p_5)^{15}N$ cross section, 0.32–1.45 MeV," Nucl. Instrum. Methods **168**, 105 (1980).
[67]J. A. Borders and J. M. Harris, "The use of $^{12}C(d, p)^{13}C$ and $^{16}O(d, p)^{17}O$ reactions to profile carbon and oxygen in solids," Nucl. Instrum. Methods **149**, 279 (1978).
[68]L. C. Northcliffe and R. F. Schilling, "Range and stopping power tables for heavy ions," Nucl. Data Tables **A7**, 233 (1970).
[69]L. G. Earwaker, "Nuclear reaction analysis of oxide layers," Nucl. Instrum. Methods **197**, 41 (1982).
[70]G. Amsel, G. Beranger, B. de Gelas, and P. Lacombe, "Use of the nuclear reaction $^{16}O(d, p)^{17}O$ to study oxygen diffusion in solids and its application to zirconium," J. Appl. Phys. **39**, 2246 (1968).
[71]H. Chen, J. Chen, C. Ren, *et al.*, "Ion beam analysis in archeology," Nucl. Instrum. Methods **191**, 391 (1981).
[72]C. Heiser, C. Bauer, H. Frey, and W. Rudolph, "Detection of carbon and oxygen by means of deuteron induced nuclear reactions," to be published in J. Radioanal. Chem.
[73]A. Turos, L. Wielunski, and A. Barcz, "Use of the nuclear reaction $^{16}O(d, \alpha)^{14}N$ in the microanalysis of oxide surface layers," Nucl. Instrum. Methods **111**, 605 (1973).
[74]S. T. Picraux, "Low-concentration oxygen depth profiling by the $^{16}O(d, \alpha)^{14}N$ reaction," Nucl. Instrum. Methods **149**, 289 (1978).
[75]J. K. Hirvonen and W. H. Lucke, "Nuclear reaction analysis of ^{16}O concentration profiles with a high resolution magnetic spectrometer," Nucl. Instrum. Methods **149**, 295 (1978).
[76]T. Joy and D. G. Barnes, "Some practical applications of the observation of the ^{16}O-direct proton capture reaction with a Ge(Li) detector," Nucl. Instrum. Methods **95**, 199 (1971).
[77]G. Debras and G. Deconninck, "Light element analysis and application to glass industry," J. Radioanal. Chem. **38**, 193 (1977).
[78]C. R. Allen, G. Dearnaley, and N. E. W. Hartley, "Quantitative measurement of light element profiles in thick corrosion films on steels, using the Harwell nuclear microbeam," in Ref. 29 Vol. 2, p. 901.
[79]J. W. McMillan and T. B. Pierce "Nuclear microprobe analysis of reactor materials," in Ref. 29, Vol. 2, p. 913.
[80]G. Weber and L. Quaglia, "Oxygen, carbon and nitrogen determination by means of nuclear reactions," J. Radioanal. Chem. **12**, 323 (1972).
[81]T. B. Pierce, J. W. McMillan, P. F. Peck, and I. G. Jones, "An examination of carbon diffusion profiles in steel specimens by means of the nuclear microprobe," Nucl. Instrum. Methods **118**, 115 (1974).
[82]J A. Davies and P. R. Norton, "Absolute coverage measurement of adsorbed CO and D_2 on platinum," Nucl. Instrum. Methods **168**, 611 (1980).
[83]W. Rudolph, C. Bauer, P. Gippner, and K. Hohmuth, "Detection of carbon contamination by means of the $^{12}C(p, \gamma)^{13}N$ resonance reaction," Nucl. Instrum. Methods **191**, 373 (1981).
[84]P. P. Pronko, P. R. Okamoto, and H. Wiedersich, "Low energy p–Be nuclear reactions for depth profiling Be in alloys," Nucl. Instrum. Methods **149**, 77 (1978).
[85]G. K. Hubler, J. Comas, and L. Plew, "Profiles of ion-implanted Be in GaAs by means of (p, α) nuclear reaction and SIMS methods," Nucl. Instrum. Methods **149**, 635 (1978).
[86]J. A. Borders, "Analysis of coatings and thin films using energetic ions," Thin Solid Films **64**, 403 (1979).
[87]C. Olivier and M. Peisach, "The determination of ^{10}B by prompt proton spectrometry," J. Radioanal. Chem. **12**, 313 (1972).
[88]A. Armigliato, G. G. Bentini, G. Ruffini, *et al.*, "Analysis of boron predeposited silicon wafers by combined ion beam techniques and x-ray microanalysis," Nucl. Instrum. Methods **149**, 653 (1978).
[89]W. Möller, M. Hufschmidt, and Th. Pfeiffer, "Diffusion studies by means of nuclear reaction depth profiling" Nucl. Instrum. Methods **149**, 73 (1978).
[90]M. Hufschmidt, W. Möller, V. Heintze, and D. Kamke, "Depth profiling of deuterons in metals at large implantation depths using the nuclear reaction technique," in Ref. 29, Vol. 2, p. 831.
[91]W. Möller, Th. Pfeiffer, and D. Kamke, "Gas reemission and blister formation on nickel surfaces during high energy deuteron bombardment," in Ref. 29, Vol. 2, p. 841.
[92]Y. Kido, M. Kakeno, K. Yamada, *et al.*, "Defect trapping of deuterium implanted in aluminum," J. Phys. F **12**, 1567 (1982).
[93]G. Amsel, E. d'Artemare, and E. Girard, "A simple digitally controlled, automatic hysteresis free, high precision energy scanning system for van de Graaff type accelerators. Part I: Principle, results and application," Nucl. Instrum. Methods **205**, 5 (1983).
[94]C. S. Lin, W. S. Hou, M. Wen, and J. C. Chou, "Cross section measurements for the $^6Li(p, \alpha)^3He$ reaction in the proton energy range 1.0–2.6 MeV," Nucl. Phys. **A275**, 93 (1977).
[95]I. Golicheff, H. Loeuillet, and Ch. Engelman, "Analytical application of the direct observation of nuclear reactions induced by low-energy protons and leading to the reactions induced by low-energy protons and leading to the emission of γ-photons, which are measured," J. Radioanal. Chem. **12**, 233 (1972).
[96]J. W. McMillan, F. C. W. Pummery, and P. M. Pollard, "Experience in the use of the Harwell nuclear microprobe," Nucl. Instrum. Methods **197**, 171 (1982).

Translated by Julian B. Barbour